

ChangeMamba: Remote Sensing Change Detection with Spatio-Temporal State Space Model

Hongruixuan Chen[†], *Student Member, IEEE*, Jian Song[†], Chengxi Han, *Student Member, IEEE*, Junshi Xia, *Senior Member, IEEE*, Naoto Yokoya, *Member, IEEE*

arXiv:2404.03425v1 [eess.IV] 4 Apr 2024

Abstract—Convolutional neural networks (CNN) and Transformers have made impressive progress in the field of remote sensing change detection (CD). However, both architectures have their inherent shortcomings. Recently, the Mamba architecture, based on spatial state models, has shown remarkable performance in a series of natural language processing tasks, which can effectively compensate for the shortcomings of the above two architectures. In this paper, we explore for the first time the potential of the Mamba architecture for remote sensing change detection tasks. We tailor the corresponding frameworks, called MambaBCD, MambaSCD, and MambaBDA, for binary change detection (BCD), semantic change detection (SCD), and building damage assessment (BDA), respectively. All three frameworks adopt the cutting-edge visual Mamba architecture as the encoder, which allows full learning of global spatial contextual information from the input images. For the change decoder, which is available in all three architectures, we propose three spatio-temporal relationship modeling mechanisms, which can be naturally combined with the Mamba architecture and fully utilize its attribute to achieve spatio-temporal interaction of multi-temporal features and obtain accurate change information. On five benchmark datasets, our proposed frameworks outperform current CNN- and Transformer-based approaches without using any complex strategies or tricks, fully demonstrating the potential of the Mamba architecture. Specifically, we obtained 83.11%, 88.39% and 94.19% F1 scores on the three BCD datasets SYSU, LEVIR-CD+, and WHU-CD; on the SCD dataset SECOND, we obtained 24.04% SeK; and on the xBD dataset, we obtained 81.41% overall F1 score. The source code will be available in <https://github.com/ChenHongruixuan/MambaCD>

Index Terms—State space model, Mamba, Binary change detection, semantic change detection, building damage assessment, spatio-temporal relationship, optical high-resolution images

I. INTRODUCTION

CHANGE detection (CD) has been a popular field within the remote sensing community since the inception of remote sensing technology. It aims to detect changes in objects

Manuscript submitted April xx, 2024. This work was supported in part by the Council for Science, Technology and Innovation (CSTI), the Cross-ministerial Strategic Innovation Promotion Program (SIP), Development of a Resilient Smart Network System against Natural Disasters (Funding agency: NIED), the JSPS, KAKENHI under Grant Number 22H03609, JST, FOREST under Grant Number JPMJFR206S, Microsoft Research Asia, and Next Generation AI Research Center, The University of Tokyo. ([†]: equal contribution; Corresponding author: Naoto Yokoya)

Hongruixuan Chen, Jian Song, and Naoto Yokoya are with Graduate School of Frontier Sciences, The University of Tokyo, Chiba, Japan (e-mail: qschrx@gmail.com; song@ms.k.u-tokyo.ac.jp; yokoya@k.u-tokyo.ac.jp).

Chengxi Han is with State Key Laboratory of Information Engineering in Surveying, Mapping, and Remote Sensing, Wuhan University, Wuhan, China (e-mail: chengxihan@whu.edu.cn).

Junshi Xia is with RIKEN Center for Advanced Intelligence Project (AIP), RIKEN, Tokyo, 103-0027, Japan (e-mail: junshi.xia@riken.jp).

on the Earth’s surface from multi-temporal remote sensing images acquired at different times. Depending on the desired result from the change detector, CD tasks can be categorized into three types, namely binary CD (BCD), semantic CD (SCD), and building damage assessment (BDA). Now, CD techniques play an important role in many fields, including land cover change analysis, urban sprawl studies, disaster response, geographic information system (GIS) updating and ecological monitoring [1]–[6].

Optical high-resolution remote sensing imagery has become one of the most applied and researched data sources in the field of CD, which can provide detailed textural and geometric structural information about surface features, allowing us to achieve more refined changes. Due to the increased heterogeneity within the same land-cover feature brought about by the increase in spatial resolution, the traditional pixel-based CD methods [7]–[9] are difficult to achieve satisfactory detection results. To cope with this, researchers proposed object-based CD methods [10], which take the object consisting of homogeneous pixels as the basic unit for CD. However, these methods rely on hand-designed “shallow” features, which are not representative and robust enough to cope with complex ground conditions in multi-temporal high-resolution images [11].

The emergence of deep learning has brought new models and paradigms for CD, greatly improving the efficiency and accuracy of CD. After the early days of developing image patch-based approaches with tiny deep learning models [12]–[14], the released of a number of large-scale benchmark datasets [15] allowed us to start designing and introducing even larger and deeper models. Convolutional neural network (CNN)-based methods have been dominant within the field of CD after the introduction of fully convolutional networks (FCNs) to the field by Daudt *et al.* [16]. By employing models within the computer vision field as well as a priori knowledge of the CD task, many representative methods have been proposed [3], [4], [17]–[19]. Despite the decent results achieved by these methods, the inherent shortcomings of the CNN model structure, i.e., the inability of the limited receptive field to capture long-range dependencies between pixels, make these methods still fall short when dealing with complex and diverse multi-temporal scenes in images with different spatial-temporal resolutions [20]. The emergence of visual Transformer [21] provides an effective way to solve the above problems. By means of the self-attention operation, the transformer architecture can efficiently model the relationship between all the pixels of the whole image. Currently, more

and more CD architectures adopt Transformer architectures as the encoder to extract representative and robust features [22]–[24] and utilize it in the decoder to capture the spatio-temporal relationship between multi-temporal features [20], [25], exhibiting superior performance.

Nonetheless, the self-attention operation requires quadratic complexity in terms of image sizes, resulting in expensive computational overhead, which is detrimental in dense prediction tasks, e.g., land-cover mapping, object detection, and CD, in large-scale remote sensing datasets. Some available solutions, such as limiting the size of the computational window or step size to improve the efficiency of attention, are at the cost of imposing limits on the size of the reception field [26], [27]. As a viable alternative to the Transformer architecture, state space sequence models (SSMs), especially structured state space sequence models (S4) [28], have shown cutting-edge performance in continuous long-sequence data analysis, with the promising attribute of linearly scaling in sequence length. The Mamba architecture [29] further improves on S4 by utilizing a selection mechanism that allows the model to select relevant information in an input-dependent manner. By combining it with hardware-aware implementations, Mamba outperforms Transformers on a number of downward exploration tasks with high efficiency. Very recently, Mamba architecture has been extended to image data and shown promising results on some visual tasks [30], [31]. However, its potential for high-resolution optical images and different CD subtasks is still under-explored. How to design a suitable architecture based on a priori knowledge of CD tasks is undoubtedly valuable for subsequent research in the community.

In this paper, we present the ChangeMamba architecture, an efficient Mamba model for remote sensing CD tasks. ChangeMamba can efficiently model the global spatial context, thereby showing very effective results on the three subtasks of CD, namely BCD, MCD, and BDA. Specifically, ChangeMamba is based on the recently proposed VMamba architecture [30], which adopts a Cross-Scan Module (CSM) to unfold image patches in different spatial directions to achieve effective modeling of global contextual information of images. In addition, since CD tasks require the detector to adequately capture the spatio-temporal relationships between multi-temporal images, we design a cross-spatio-temporal state space module (CST-Mamba), which can adequately model the spatio-temporal relationships between multi-temporal features by combining them in different ways, and thus efficiently detect the different categories of changes, including binary changes, semantic changes, and building damage levels.

In summary, the main contributions of this paper are as follows:

- 1) For the first time, we explore the application of the Mamba architecture in the field of remote sensing change detection, thereby achieving high accuracy and efficient CD.
- 2) Based on the Mamba architecture and incorporating the unique characteristics of CD, we design the corresponding network frameworks for each of the three CD tasks: BCD, SCD, and BDA.

- 3) Three spatio-temporal relationship modeling mechanisms are proposed, tailored for CD tasks, with the aid of the Mamba architecture to fully learn spatio-temporal features.
- 4) The proposed three frameworks show very competitive and even SOTA performance on BCD, SCD, and BDA tasks on five benchmark datasets, demonstrating their superiority. The source code for this work is publicly available for contributions to subsequent possible research.

The remainder of this paper is organized as follows. Section II reviews related work. Section III elaborates on the three ChangeMamba architectures proposed for BCD, MCD, and BDA, respectively. The experimental results and discussion are provided in Sections IV. Section V draws the conclusion.

II. RELATED WORKS

In this section, we focus on reviewing deep learning-based CD methods concentrating on optical high-resolution remote sensing images as data sources.

A. CNN-Based Method

The rapid evolution of CNN and their prowess in extracting local features have led to early applications in CD tasks. In the realm of CNN-based BCD, an initial and simple approach [16] involved combining bi-temporal images into a single input for processing by an FCN. In addition, it introduced two variations that employ siamese encoders to handle dual inputs. Given the roots of FCNs in semantic segmentation, [17] sought to tailor these networks more closely to BCD tasks by integrating feature change maps as a deep supervised signal, thus refining the final prediction. Addressing the limited receptive field of CNNs, [13] expanded this framework by combining long- and short-term memory (LSTM) networks with CNNs. Furthermore, Fang *et al.* [32] designed a Siamese architecture with denser connections to facilitate more effective shallow information exchange for BCD. To combat the challenge of uneven foreground-background distributions within BCD, Han *et al.* [33] employed a novel sampling approach and an attention mechanism to integrate global information more effectively. After that, they further introduced an innovative self-attention module that not only enhances long-distance dependency, but also specifically targets the refinement of BCD predictions, significantly improving the delineation of change area boundaries and reducing the occurrence of inner holes [34].

Compared to BCD, which aims to identify "where" changes have occurred, SCD seeks to determine "what" the changes are. Although this poses a greater challenge, it is more important for downstream applications in remote sensing. In the field of CNN-based SCD, FCNs remain the core structure. Early explorations in SCD include [35], which adopts a multitask learning framework to simultaneously predict a binary change mask and land cover mapping, using the latter to assist in generating the final semantic change prediction. The approach in [36] represents an early attempt to combine recurrent neural network (RNN) and CNN with SCD, where

CNN extracts semantic features and RNN models temporal dependencies to classify multiple types of changes. In [37] and [11], unsupervised SCD methods were developed, using pre-trained CNNs or unsupervised learning techniques to extract temporal features, then comparing these features to classify changes. [38] introduced a benchmark dataset for SCD along with a new evaluation metric. Building on [35], Ding *et al.* [39] proposed a more innovative architecture to address the insufficient exchange of information between the semantic and change branches, introducing new loss functions and supervision signals to force the network to correlate two branches. Zheng *et al.* [18] continues to strengthen the connection between the two branches, designing a temporal-symmetric transformer (TST) module to model the causal relationship between semantic and change representations. In [40], channel attention is used to embed change information into temporal features. In [41], temporal salient features are used and fused to extract and improve the representation of changes.

Compared to the advances in CNN-based methods for BCD and SCD, the progression of BDA methodologies has been relatively gradual. BDA intricately categorizes areas affected by disasters into four distinct classes: "No damage", "Minor damage", "Major damage", and "Destroyed". The procedural approach to BDA typically encompasses two primary phases: identifying the location of the building and assessing the level of damage incurred. This bifurcation essentially positions BDA as a nuanced subset of SCD, with a focus on quantifying damage levels. Among established approaches, the xView2 challenge [42] introduced a baseline method that employs a UNet+ResNet cascade for building localization and damage classification, trained with pre and post-disaster imagery. The Siamese-UNet, the winning approach of the xView2 challenge [42], utilizes a UNet framework for both pixel-level building localization and damage level classification. It innovatively initializes the damage classification UNet with the parameters from the building localization UNet, enhancing performance through a multi-model ensemble of four UNets. Further advancements [43] draw from SCD solutions and the Mask-RCNN architecture to address BDA, incorporating Siamese encoders, multitask heads, and instance-level predictions. An evolved approach [3] introduces a hybrid encoder architecture that merges shared and task-specific weights, alongside an FCN-based multitask decoder. This development enhances task integration with an object-based post-processing strategy, resulting in more refined outcomes.

The development of CNN-based CD methods has matured significantly over time. However, despite their excellent ability to extract local features, CNN architectures inherently struggle to capture long-distance dependencies. This limitation becomes particularly critical in CD tasks, where change regions, compared to background areas, are often sparse and scattered. The network's ability to model relationships beyond local areas is essential for accurately identifying these change regions. In this context, Mamba, evolved from RNN architectures, stands out for its exceptional ability to model non-local relationships, making it ideally suited for CD tasks. Its architecture leverages the sequential processing strength of RNNs, enabling it to effectively understand the spatial context

and dependencies over larger areas, thus overcoming one of the key limitations of traditional CNN-based approaches in CD.

B. Transformer-Based Method

Recently, with the rise of transformers in computer vision tasks, their superior long-distance modeling capabilities, compared to CNNs, have made them particularly effective in the field of BCD, SCD, and BDA. In the realm of BCD, [20] emerges as a pioneering approach, transforming images into semantic tokens to model spatial-temporal contexts within a token-based framework, enhancing the change detection process. Bandara *et al.* [22] employing a pure transformer-based Siamese network that uses a structured transformer encoder coupled with an MLP decoder. This architecture eliminates the need for a CNN-based feature extractor. At the same time, Zhang *et al.* [24] also proposes a pure transformer-driven model, adopting a Siamese U-shaped structure, processing images in parallel to extract and merge multiscale features. It leverages Swin transformer blocks across its architecture, further demonstrating the transformer's capability to refine change detection outcomes. Li *et al.* [25] introduces a hybrid model that blends understanding of the global context of transformers with the semantic detail resolution of UNet. It eliminates UNet's redundant information and enhances feature quality through a difference enhancement module, leading to more precise change area delineation.

As for transformer-based SCD, Niu *et al.* [44] uses a PRTB backbone, combining preactivated residual and transformer blocks, to extract semantic features from image pairs, which is crucial for detecting subtle changes. Its Multi-Content Fusion Module (MCFM) precisely differentiates between the foreground and background. The model's efficacy is further amplified by multitask prediction branches and a custom loss function, ensuring nuanced semantic change detection with heightened accuracy. Alternatively, Ding *et al.* [45] introduces the Semantic Change Transformer (SCanFormer), a CSWin Transformer adaptation, to explicitly chart semantic transitions. The model utilizes a triple encoder-decoder architecture to improve spatial features, and it is distinguished by incorporating spatio-temporal dynamics and task-specific expertise, leading to a decrease in learning disparities. This approach significantly boosts accuracy on benchmarks, adeptly managing scenarios with sparse change samples and semantic labels.

In response to the transformer-based BDA, Chen *et al.* [23] uses a siamese Mix Transformer (MiT) encoder and lightweight All-MLP decoder efficiently to process bi-temporal image pairs. It features deep feature extraction and a multitemporal fusion module for improved information integration, and a dual-task decoder for precise building localization and damage classification. By adopting strategies like weight sharing and innovative fusion mechanisms, it efficiently handles high-resolution imagery with lower computational costs, making it effective and streamlined for BDA.

Although transformer-based methods have significantly enhanced CD accuracy through their powerful non-local modeling capabilities, they come with substantial computational

resource demands. Specifically, as the number of tokens increases, the consumption of computational resources escalates quadratically, posing challenges for processing large-scale input. However, Mamba, an architecture inherited from RNNs, not only rivals transformers in non-local modeling capabilities but also maintains computational resource consumption at a linear growth rate.

Moreover, spatio-temporal fusion remains a fundamental aspect of CD tasks, where seamless and efficient integration of time and space information is essential to achieve accurate detection results. Traditional methods, whether they employ CNNs or transformers, tend to follow a rigid, modular stacking approach for spatio-temporal fusion. In contrast, the Mamba framework introduces a novel paradigm by treating tokens with inherent "sequence," offering a dynamic range of spatio-temporal fusion possibilities. By manipulating the order in which tokens are processed, Mamba can generate a spectrum of fusion outcomes, marking a significant departure from conventional methods. This innovative approach to spatiotemporal fusion provides Mamba with unparalleled flexibility and effectiveness in addressing CD tasks.

C. State Space Model

The SSM concept first popped up with the S4 model [28], offering a new way to handle contextual information globally, which caught attention because of its attractive property of scaling linearly in sequence length. Based on S4, Smith et al. [46] proposed a new S5 model by introducing MIMO SSM and efficient parallel scan into the S4 model. After that, the H3 model [47] further advanced these concepts, achieving performance on par with Transformers in language modeling tasks. Recently, Gu et al [29] proposed a data-dependent SSM layer and built a generic language model backbone called Mamba, which outperforms Transformers at different scales on large-scale real data and scales linearly in sequence length. Very recently, VMamba [30] and Vision Mamba [31] have extended Mamba architecture to 2D image data, showing superior performance on many computer vision tasks. Inspired by this progress, some pioneering work has introduced the Mamba architecture to the field of remote sensing image processing [48], [49]. Their studies show that the Mamba architecture can yield comparable performance to the advanced CNN and Transformer architectures on scene classification [49] and pansharpening [48] tasks. However, these works still focus on either low-level tasks or classification tasks, and all of these tasks are single-temporal tasks [50]. The potential of the Mamba architecture for multi-temporal remote sensing image-related scenarios and intensive prediction tasks remains to be explored.

III. METHODOLOGY

A. Preliminaries

The SSM-based models and Mamba are inspired by the linear time-invariant systems, which map a 1-D function or sequence $x(t) \in \mathcal{R}$ to response $y(t) \in \mathcal{R}$ through a hidden

state $h(t) \in \mathcal{R}^N$. These systems are usually formulated as linear ordinary differential equations (ODEs) as

$$\begin{cases} h'(t) = \mathbf{A}h(t) + \mathbf{B}x(t) \\ y(t) = \mathbf{C}h(t) \end{cases} \quad (1)$$

where $\mathbf{A} \in \mathcal{R}^{N \times N}$ is the evolution parameter and $\mathbf{B} \in \mathcal{R}^{N \times 1}$, $\mathbf{C} \in \mathcal{R}^{1 \times N}$ are the projection parameters.

The S4 and Mamba models are discrete counterparts of the continuous system as continuous systems face significant challenges when integrated into deep learning algorithms. They contain a time scale parameter Δ which is used to convert the continuous parameters \mathbf{A} and \mathbf{B} into their discrete counterparts $\bar{\mathbf{A}}$ and $\bar{\mathbf{B}}$. A prevalent way to achieve this transformation is to use a zero-order hold (ZOH) approach:

$$\begin{cases} \bar{\mathbf{A}} = \exp(\Delta \mathbf{A}) \\ \bar{\mathbf{B}} = (\Delta \mathbf{A})^{-1} (\exp(\Delta \mathbf{A}) - \mathbf{I}) \Delta \mathbf{B} \end{cases} \quad (2)$$

After that, the discretization of Eq. (1) can be formulated as

$$\begin{cases} h'_t = \bar{\mathbf{A}}h_{t-1} + \bar{\mathbf{B}}x_t \\ y_t = \mathbf{C}h_t \end{cases} \quad (3)$$

Finally, the output of x with sequence length \mathbf{L}_x can be calculated directly by the following global convolution operation

$$\begin{cases} \bar{\mathbf{K}} = (\mathbf{C}\bar{\mathbf{B}}, \mathbf{C}\bar{\mathbf{A}}\bar{\mathbf{B}}, \dots, \mathbf{C}\bar{\mathbf{A}}^{\mathbf{L}_x-1}\bar{\mathbf{B}}) \\ y = \mathbf{x} * \bar{\mathbf{K}} \end{cases} \quad (4)$$

where $\bar{\mathbf{K}} \in \mathcal{R}^{\mathbf{L}_x}$ is a structured convolutional kernel and $*$ denotes a convolutional operation.

B. Problem Statement

In this paper, we focus on three sub-tasks within the CD field. They are binary change detection (BCD), semantic change detection (SCD), and building damage assessment (BDA). The definitions of the three tasks are as follows.

1) *Binary Change Detection*: BCD is the basic and the most intensively studied task in the CD field. It focuses on "where" change occurs. According to the class of interest, BCD can also be categorized into class-agnostic CD focusing on general land-cover change information, and single-class object CD, e.g., building CD. Given a training set represented as $\mathcal{D}_{train}^{bcd} = \left\{ \left(\mathbf{X}_i^{T_1}, \mathbf{X}_i^{T_2}, \mathbf{Y}_i^{bcd} \right) \right\}_{i=1}^{N_{train}}$, where $\mathbf{X}_i^{T_1}, \mathbf{X}_i^{T_2} \in \mathcal{R}^{H \times W \times C}$ is the i -th multi-temporal image pair acquired in T_1 and T_2 , respectively, and $\mathbf{Y}_i^{bcd} \in \{0, 1\}^{H \times W}$ is the corresponding label, the goal of BCD is to train a change detector \mathcal{F}_θ^{bcd} on $\mathcal{D}_{train}^{bcd}$ that can predict change maps reflecting accurate "change / non-change" binary information on new sets.

2) *Semantic Change Detection*: Compared to BCD, SCD focuses not only on "where" the change occurs, but also on the "what" of the change, i.e. "from-to" semantic change information [18], [39], [45]. The training set in SCD task can be represented as

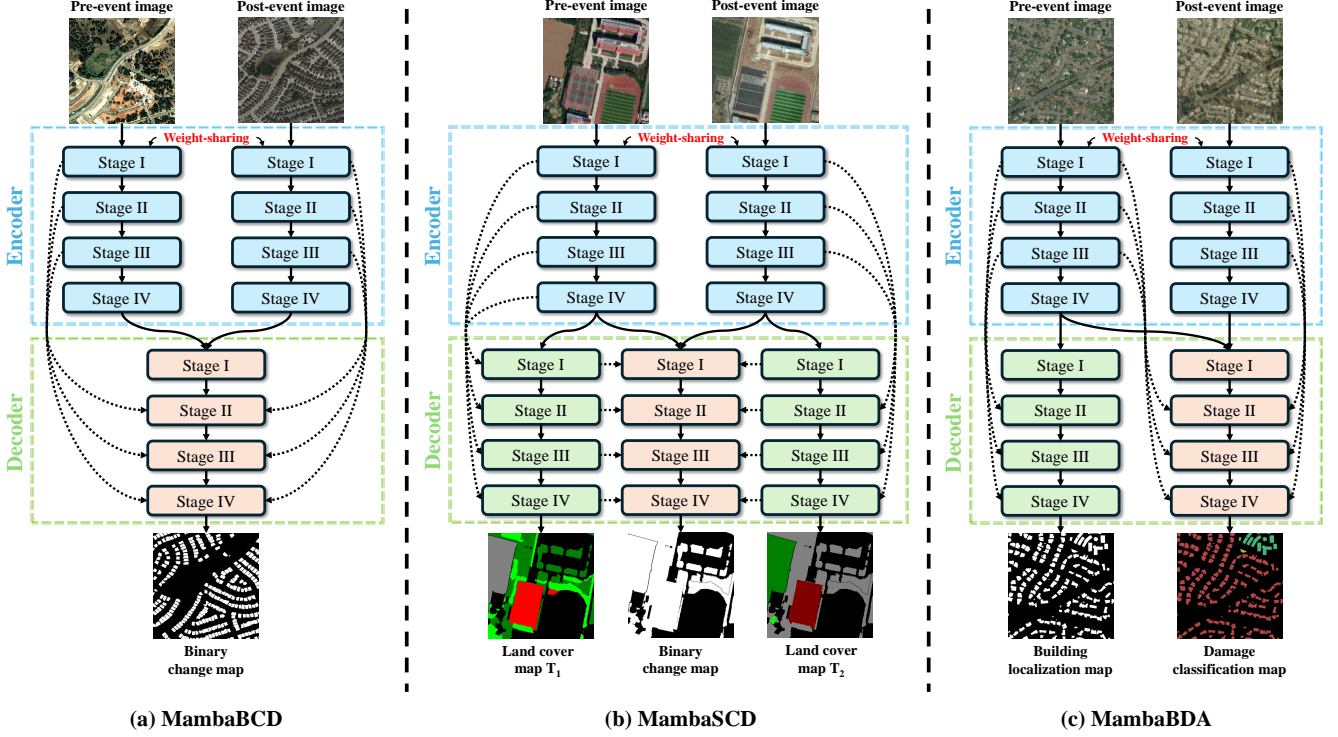


Fig. 1: The network framework of the proposed (a) MambaBCD for binary change detection, (b) MambaSCD for semantic change detection, and (c) MamabaBDA for building damage assessment.

$\mathcal{D}_{train}^{scd} = \left\{ \left(\mathbf{X}_i^{T_1}, \mathbf{X}_i^{T_2}, \mathbf{Y}_i^{T_1}, \mathbf{Y}_i^{T_2}, \mathbf{Y}_i^{bcd} \right) \right\}_{i=1}^{N_{train}}$. Compared to BCD, corresponding land-cover labels $\mathbf{Y}_i^{T_1}, \mathbf{Y}_i^{T_2} \in \{0, 1, \dots, C\}^{H \times W}$ with C categories of $\mathbf{X}_i^{T_1}$ and $\mathbf{X}_i^{T_2}$ are additionally required. The goal of SCD is to train a semantic change detector \mathcal{T}_θ^{scd} on $\mathcal{F}_{train}^{scd}$ that can predict land-cover maps of multi-temporal images and binary change maps between them on new sets as accurately as possible. By combining the information in predicted land-cover maps and binary change maps, the “from-to” semantic change information can be derived.

3) *Building Damage Assessment*: BDA is a special “one-to-many” SCD task [3]. BDA requires recognizing not only the where of the change (damage) occurs but also post-event states of the object (building) in the condition that the pre-event state of the object is unique. The training set in BDA task can be denoted as $\mathcal{D}_{train}^{bda} = \left\{ \left(\mathbf{X}_i^{T_1}, \mathbf{X}_i^{T_2}, \mathbf{Y}_i^{loc}, \mathbf{Y}_i^{clf} \right) \right\}_{i=1}^{N_{train}}$, where $\mathbf{Y}_i^{loc} \in \{0, 1\}^{H \times W}$ is the label of the object of interest (building) at T_1 , and $\mathbf{Y}_i^{clf} \in \{0, 1, \dots, C\}^{H \times W}$ is the post-event state (damage level) of the object of interest at T_2 .

C. Network Architecture

For these three CD subtasks, we design corresponding network frameworks based on the Mamba architecture, called MambaBCD, MambaSCD, and MamabBDA, respectively. Fig. 1 shows the network framework of these three architectures. Among them, the encoders of the three networks are weight-sharing siamese networks based on the Visual State Space Model (VMamba) architecture [30]. VMamba can adequately

extract the robust and representative features of the input images benefiting from the Mamba architecture and an efficient 2D cross-scan mechanism (as shown in Fig. 3). Its specific structure will be introduced in Section III-D.

1) *MambaBCD*: MambaBCD is the architecture designed for the BCD task. First, the siamese encoder network \mathcal{F}_θ^{enc} extracts multi-level features from the input image as $\left\{ \mathbf{F}_{i,j}^{T_1} \right\}_{j=1}^4 = \mathcal{F}_\theta^{enc}(\mathbf{X}_i^{T_1})$ and $\left\{ \mathbf{F}_{i,j}^{T_2} \right\}_{j=1}^4 = \mathcal{F}_\theta^{enc}(\mathbf{X}_i^{T_2})$. Next, these multi-level features are fed into a tailored change decoder $\mathcal{F}_\theta^{cdec}$. Based on the Mamba architecture, the change decoder can fully learn the spatio-temporal relationship from multi-level features through three different mechanisms, and gradually obtains an accurate BCD result, formulated as $\mathbf{P}_i^{bcd} = \mathcal{F}_\theta^{cdec} \left(\left\{ \mathbf{F}_{i,j}^{T_1} \right\}_{j=1}^4, \left\{ \mathbf{F}_{i,j}^{T_2} \right\}_{j=1}^4 \right)$. The binary change map can be obtained as $\hat{\mathbf{Y}}_i^{bcd} = \text{argmax}_c \mathbf{P}_i^{bcd}$.

2) *MambaSCD*: MambaSCD is the architecture designed for SCD tasks. As shown in Fig. 1-(b), MambaSCD adds two semantic decoders for land cover mapping tasks based on MambaBCD, denoted as $\mathcal{F}_\theta^{T_1}$ and $\mathcal{F}_\theta^{T_2}$. In addition to be treated as input as $\mathcal{F}_\theta^{cdec}$ to learn spatio-temporal relationships to predict BCD results, the multi-level features extracted by the encoder are also fed into $\mathcal{F}_\theta^{T_1}$ and $\mathcal{F}_\theta^{T_2}$ to predict the land-cover map of the corresponding temporal image, formulated as $\mathbf{P}_i^{T_1} = \mathcal{F}_\theta^{T_1} \left(\left\{ \mathbf{F}_{i,j}^{T_1} \right\}_{j=1}^4 \right)$ and $\mathbf{P}_i^{T_2} = \mathcal{F}_\theta^{T_2} \left(\left\{ \mathbf{F}_{i,j}^{T_2} \right\}_{j=1}^4 \right)$. After obtaining the land-cover maps $\hat{\mathbf{Y}}_i^{T_1} = \text{argmax}_c \mathbf{P}_i^{T_1}$ and $\hat{\mathbf{Y}}_i^{T_2} = \text{argmax}_c \mathbf{P}_i^{T_2}$ and the binary change map \mathbf{CM}_i , the semantic change information of $T_1 \rightarrow T_2$ can be obtained by performing the mask operation on $\hat{\mathbf{Y}}_i^{T_1}$ and $\hat{\mathbf{Y}}_i^{T_2}$ using $\hat{\mathbf{Y}}_i^{bcd}$.

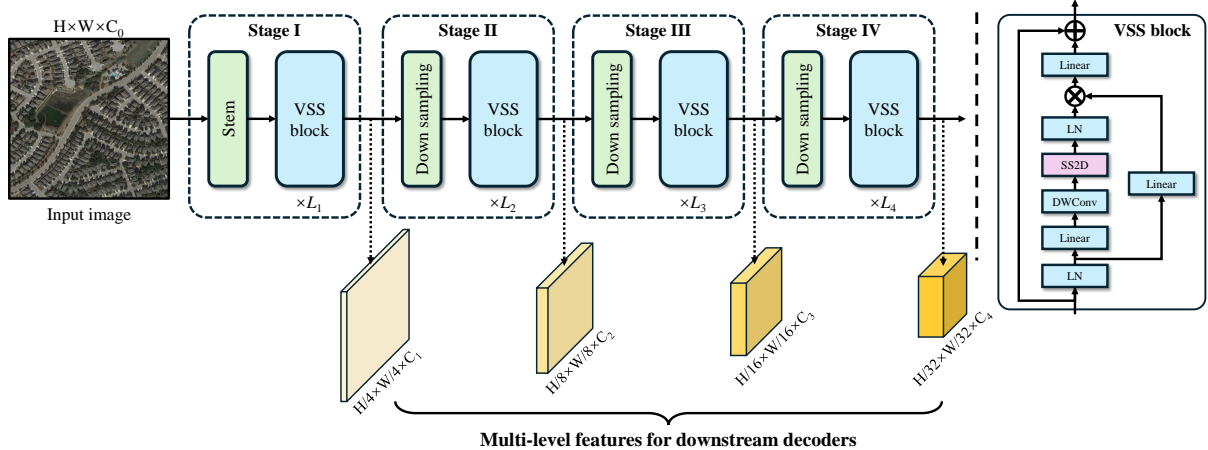


Fig. 2: The specific structure of the encoder network is based on the visual state space model used in our three architectures.

3) *MambaBDA*: MambaBDA is the architecture presented for the BDA task. Unlike the typical SCD task, the BDA task only needs to predict land-cover maps (building location maps) for pre-event images. Therefore, in the MambaBDA architecture shown in Fig. 1-(c), there is only one semantic decoder \mathcal{F}_θ^{loc} for predicting building localization map as $\mathbf{P}_i^{loc} = \mathcal{F}_\theta^{loc} \left(\left\{ \mathbf{F}_{i,j}^{\text{T}_1} \right\}_{j=1}^4 \right)$. Like MambaBCD and MambaSCD, a change decoder denoted as \mathcal{F}_θ^{clf} then learns spatio-temporal relationships from multi-temporal features to classify the damage level of buildings as $\mathbf{P}_i^{clf} = \mathcal{F}_\theta^{clf} \left(\left\{ \mathbf{F}_{i,j}^{\text{T}_1} \right\}_{j=1}^4, \left\{ \mathbf{F}_{i,j}^{\text{T}_2} \right\}_{j=1}^4 \right)$. The obtained building location map $\hat{\mathbf{Y}}_i^{loc} = \text{argmax}_c \mathbf{P}_i^{loc}$ can be used for further post-processing on the obtained damage classification map $\hat{\mathbf{Y}}_i^{clf} = \text{argmax}_c \mathbf{P}_i^{clf}$ to improve the accuracy, e.g., object-based post-processing methods [3].

D. Encoder Based on Visual State Space Model

S6 model in Mamba causally processes the input data, and thus can only capture information within the scanned part of the data. This attribute naturally aligns with natural language data, which but poses significant challenges when adapting to non-causal data such as image. Directly expanding image data along a certain dimension of space and inputting it into the S6 model will result in spatial context information not being adequately modeled. Recently, visual Mamba solved this problem well by proposing a 2D Cross-Scan mechanism. As shown in Fig. 3, before inputting the tokens into the S6 model, the cross-scan mechanism rearranges the tokens in spatial dimensions, i.e., top-left to bottom-right, bottom-right to top-left, top-right to bottom-left, and bottom-left to top-right. Finally, the resulting features are then merged. In this way, any pixel can get spatial context information from different directions. Moreover, the computational complexity of the Mamba model under the cross-scan mechanism is still $O(N)$ compared to the self-attention technique in Transformer.

Based on the Visual Mamba architecture, the specific structure of the encoder network in our proposed three architectures is shown in Fig. 2. There are four stages, each of which

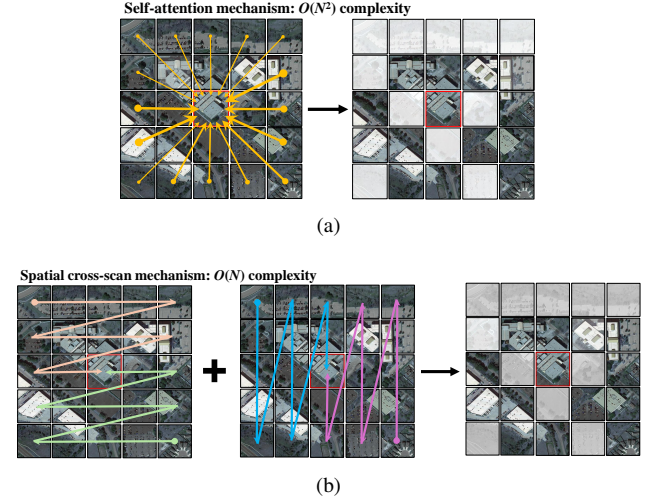


Fig. 3: Illustration of the self-attention mechanism [21], [51] and cross-scan mechanism [30] for capturing global contextual information.

first downsamples the input data, then fully models the spatial contextual information using a number of visual state space (VSS) blocks, and then outputs the features for that stage, i.e., $\mathbf{F}_{i,j}$. The structure of VSS block is also depicted in Fig. 2. The input first passes through a linear embedding layer, and the output splits into two information flows. One flow passes through a 3×3 depth-wise convolution (DWConv) layer, followed by a Silu activation function [52] before entering the core SS2D module (i.e., the integration of S6 with the cross-scan mechanism). The output of the SS2D module passes through a layer normalization (LN) layer, and is then summed up with the outputs of the other streams that have been activated by Silu. This combination produces the final output of the VSS block. Finally, the features from the four stages $\{\mathbf{F}_{i,j}\}_{j=1}^4$ are then used in the subsequent decoders responsible for specific tasks.

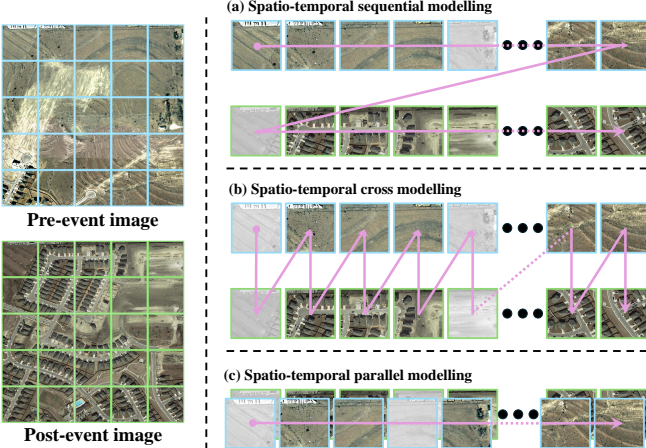


Fig. 4: Illustration of three mechanisms for learning spatio-temporal relationships based on the state space model proposed in this paper.

E. Task-Specific Decoders

1) *Spatio-Temporal Relationship Modelling Mechanism*: Although the employed encoder can extract robust and representative features, learning spatio-temporal relationships of multi-temporal images is also significant to CD tasks [18], [36]. To this end, we propose three mechanisms for modeling spatio-temporal relationships that can be aligned with the attribute of the S6 model capable of adequately modeling the global contextual information of long sequential data. Fig. 4 illustrates the three modeling mechanisms. They are spatio-temporal sequential modelling, spatio-temporal cross modeling, and spatial-temporal parallel modeling. Sequential modelling is unfolding the tokens of two temporal phases of data and then arranging them in temporal order as $F_{i,j}^s = [F_{i,j}^{T_1}(1), \dots, F_{i,j}^{T_1}(HW/2^{1+j}), F_{i,j}^{T_2}(1), \dots, F_{i,j}^{T_2}(HW/2^{1+j})]$. Cross modelling mechanism, on the other hand, is modeling by cross-ordering the tokens of the two temporal phases as $F_{i,j}^s = [F_{i,j}^{T_1}(1), F_{i,j}^{T_2}(1), \dots, F_{i,j}^{T_1}(HW/2^{1+j}), F_{i,j}^{T_2}(HW/2^{1+j})]$. Finally, parallel modeling is done by concatenating the tokens of the two temporal phases in the channel dimension and then performing joint modeling, i.e., $F_{i,j}^p = \text{concat}_c([F_{i,j}^{T_1}, F_{i,j}^{T_2}])$. Through these three mechanisms and Mamba architecture, the spatio-temporal relationships intrinsic in the multi-temporal features will be fully explored, helping the decoder to obtain accurate change detection results.

2) *Change Decoder*: Based on the proposed three spatio-temporal learning mechanisms, the specific structure of the change decoder is then shown in Fig. 5. It fully learns the spatio-temporal relationships from the extracted multi-temporal features $\{F_{i,j}^{T_1}\}_{j=1}^4$ and $\{F_{i,j}^{T_2}\}_{j=1}^4$ in four stages and obtains accurate binary change maps. At the beginning of each stage, the spatio-temporal relationship of multi-temporal features is first modeled using an STSS block. In the STSS block, a spatio-temporal tokens generator module will rearrange the input multi-temporal features, which are then fed into three VSS blocks. Each block is responsible for learning one of the spatio-temporal relationships in Fig. 4. The output

of the STSS block of the current stage is then integrated with the information from the feature map of the previous stage through a fusion module. After passing through an upsampling layer, the feature map is fed to the next stage.

3) *Semantic Decoder*: The specific structure of the semantic decoder is then shown in Fig. 6. It is mainly responsible for gradually recovering the class-agnostic or object-specific land-cover maps of the corresponding multi-level features extracted by the encoder. It also has four stages. At the beginning of each stage, the global spatial context information of input data is first modeled using a VSS block. Then the feature map is up-sampled and integrated with information about the lower-level feature map with higher resolution through a fusion module. In the fusion module, the number of channels of the low-level feature map is mapped to be consistent with the high-level feature map by a 1×1 convolutional layer. Then the high-level and low-level feature maps are summed. Finally, the resulting feature map is smoothed by a residual layer.

F. Loss Function

Since this paper focuses on exploring the potential of the Mamba architecture for CD, we have optimized networks using commonly used loss functions in the field. Some tricks for improving accuracy like focal loss [53], deep supervision [17], multi-scale training/testing [6], etc. are not adopted. Nevertheless, in the experimental section, we can find that the proposed architecture achieves very competitive and even SOTA performance on all three subtasks.

1) *BCD*: Since BCD can be regarded as a special semantic segmentation task [50], we directly optimize the network using cross-entropy loss as

$$\mathcal{L}_{ce}^{bcd} = -\frac{1}{N_{train}^{bcd}} \sum_{i=1}^{N_{train}^{bcd}} \sum_{c=0}^1 \tilde{\mathbf{Y}}_i^{bcd}(c) \log(\mathbf{P}_i^{bcd}(c)), \quad (5)$$

where $\tilde{\mathbf{Y}}_i^{bcd}$ is the one-hot form of \mathbf{Y}_i^{bcd} , $\mathbf{P}_i^{bcd} = \mathcal{F}_\theta^{bcd}(\mathbf{X}_i^{T_1}, \mathbf{X}_i^{T_2})$ is the output of the binary change detector through the softmax activation.

In addition, the Lovasz-softmax loss [54] is introduced to alleviate the problem of imbalance in the number of samples between changed and unchanged pixels. The final loss function for the BCD task is formulated as

$$\mathcal{L}_{final}^{bcd} = \mathcal{L}_{ce}^{bcd} + \mathcal{L}_{lov}^{bcd}. \quad (6)$$

2) *SCD*: For the SCD task, in addition to optimizing the BCD task, it is also necessary to optimize the land cover mapping task for both pre-event and post-event images, which can be optimized with cross-entropy loss as

$$\begin{cases} \mathcal{L}_{ce}^{T_1} = -\frac{1}{N_{train}^{scd}} \sum_{i=1}^{N_{train}^{scd}} \sum_{c=0}^C \tilde{\mathbf{Y}}_i^{T_1}(c) \log(\mathbf{P}_i^{T_1}(c)) \\ \mathcal{L}_{ce}^{T_2} = -\frac{1}{N_{train}^{scd}} \sum_{i=1}^{N_{train}^{scd}} \sum_{c=0}^C \tilde{\mathbf{Y}}_i^{T_2}(c) \log(\mathbf{P}_i^{T_2}(c)) \end{cases}, \quad (7)$$

where $\mathbf{P}_i^{T_1}$ and $\mathbf{P}_i^{T_2}$ are the probabilistic map of land-cover classification for the pre-event image and post-event

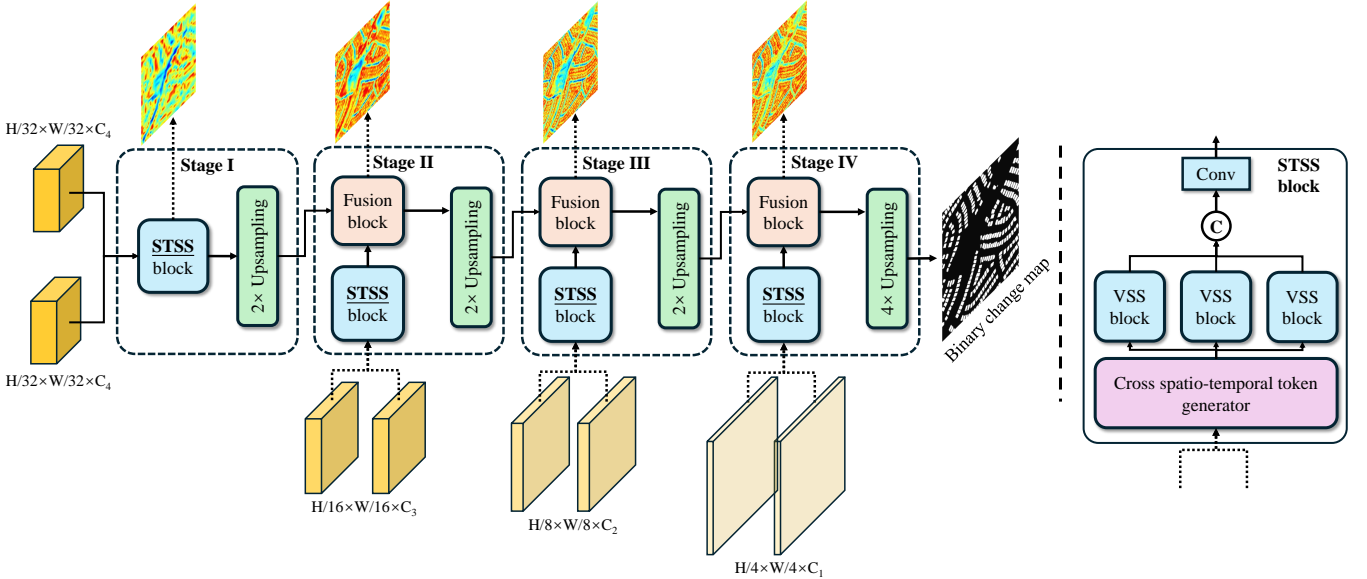


Fig. 5: The specific structure of the change decoder used in MambaBCD, MambaSCD, and MambaBDA architectures.

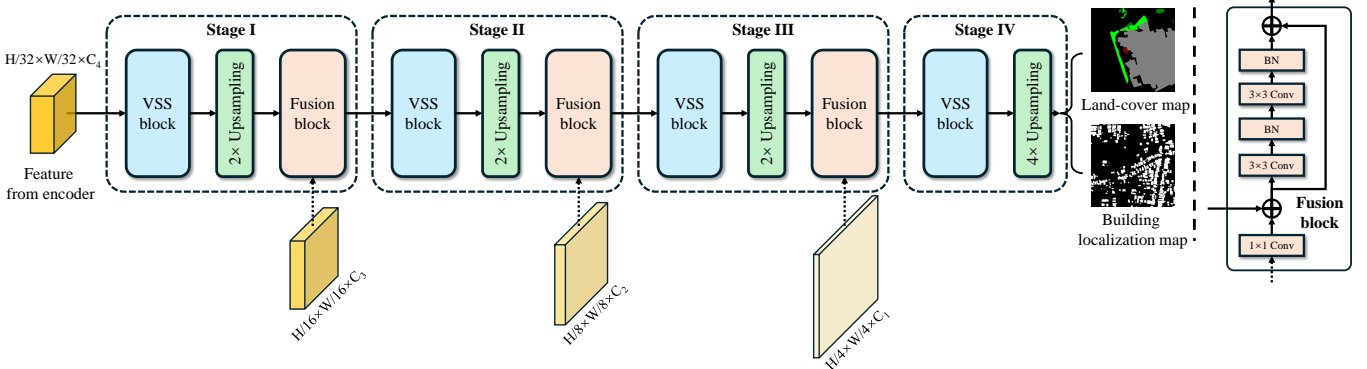


Fig. 6: The specific structure of the semantic decoder in MambaSCD and MambaBDA architectures.

image output by the semantic decoder of the MambaSCD architecture; $\mathcal{L}_{ce}^{T_1}$ and $\mathcal{L}_{ce}^{T_2}$ are the corresponding cross-entropy loss.

Similarly, the Lovasz-softmax loss function is used to solve the sample imbalance problem. Thus, the final loss function for the SCD task takes the form

$$\mathcal{L}_{final}^{scd} = \mathcal{L}_{ce}^{bcd} + \mathcal{L}_{lov}^{bcd} + \frac{1}{2} (\mathcal{L}_{ce}^{T_1} + \mathcal{L}_{ce}^{T_2} + \mathcal{L}_{lov}^{T_1} + \mathcal{L}_{lov}^{T_2}). \quad (8)$$

3) BDA: BDA contains a building location task and a building damage classification task. The cross-entropy loss for each task can be expressed as follows

$$\begin{cases} \mathcal{L}_{ce}^{loc} = -\frac{1}{N_{train}^{bda}} \sum_{i=1}^{N_{train}^{bda}} \sum_{c=0}^C \tilde{\mathbf{Y}}_i^{loc}(c) \log(\mathbf{P}_i^{loc}(c)) \\ \mathcal{L}_{ce}^{clf} = -\frac{1}{N_{train}^{bda}} \sum_{i=1}^{N_{train}^{bda}} \sum_{c=0}^C \tilde{\mathbf{Y}}_i^{clf}(c) \log(\mathbf{P}_i^{clf}(c)) \end{cases}, \quad (9)$$

where \mathbf{P}_i^{loc} and \mathbf{P}_i^{clf} are the output of localization branch and classification branch of the MambaBDA architecture, respectively; \mathcal{L}_{ce}^{loc} and \mathcal{L}_{ce}^{clf} are the corresponding cross-entropy

loss of building localization and damage classification tasks, respectively.

By utilizing the Lovasz-softmax loss function to solve the sample imbalance problem, the final loss function of BDA is formulated as

$$\mathcal{L}_{final}^{bda} = \mathcal{L}_{ce}^{loc} + \mathcal{L}_{lov}^{loc} + \mathcal{L}_{ce}^{clf} + \mathcal{L}_{lov}^{clf}. \quad (10)$$

IV. EXPERIMENTS AND DISCUSSIONS

A. Datasets

1) SYSU-CD [15]: This dataset introduces a comprehensive collection of 20,000 pairs of 0.5-meter resolution aerial images from Hong Kong, spanning 2007 to 2014, to advance the field of CD. This dataset is distinguished by its focus on urban and coastal changes, featuring high-rise buildings and infrastructure developments, areas where CD poses significant challenges due to shadow and deviation effects. For effective deep learning (DL) application, the dataset is structured into training, validation, and test sets following a 6:2:2 ratio, with 20,000 patches of 256×256 . Covering diverse change scenarios such as urban construction, suburban expansion,

groundwork, vegetation changes, road expansion, and sea construction, the SYSU-CD dataset is positioned as a pivotal resource for CD research.

2) *WHU-CD* [55]: The WHU-CD dataset, a segment of the larger WHU Building dataset, is tailored for the task of building change detection. It comprises two aerial datasets from Christchurch, New Zealand, captured in April 2012 and 2016, with a high image resolution of 0.3m. This dataset is particularly focused on detecting changes in large and sparse building structures. The 2012 dataset includes aerial imagery covering an area of 20.5 km², featuring 12,796 buildings, while the 2016 dataset shows an increase to 16,077 buildings within the same area, reflecting significant urban development over the four-year period. We cropped these large training (21,243 × 15,354) and testing (11,265 × 15,354) images into non-overlapping 256 × 256 patches for our experiments.

3) *LEVIR-CD+* [56]: This advanced version of the LEVIR-CD dataset introduces a comprehensive resource for BCD research. It comprises 985 pairs of very high-resolution Google Earth images at 0.5m/pixel resolution, each with dimensions of 1024 × 1024 pixels. Spanning a time interval of 5 to 14 years, these bi-temporal images document significant building construction changes. It also encompasses a wide array of building types, including villa residences, tall apartments, small garages, and large warehouses, with a focus on both the emergence of new buildings and the decline of existing structures. The dataset is meticulously annotated with binary labels by experts in remote sensing image interpretation. Each image pair undergoes a rigorous two-step quality assurance process involving initial annotation and subsequent verification to ensure the accuracy of change instances. The final dataset features 31,333 instances of building changes, making LEVIR-CD+ a valuable benchmark for evaluating CD methodologies.

4) *SECOND* [38]: The SECOND dataset introduces a collection of 4,662 pairs of 512 × 512 aerial images at 0.5-3m/pixel resolution, annotated for SCD in cities such as Hangzhou, Chengdu, and Shanghai. It focuses on six primary land cover classes: non-vegetated ground surfaces, trees, low vegetation, water, buildings, and playgrounds to capture a wide range of geographical changes. Annotations are done by experts, ensuring high accuracy at the pixel level. The dataset uses land-cover map pairs and non-change masks to accurately represent change, facilitating the differentiation of changes from unchanged pixels within the same class. This methodological approach ensures its utility in addressing SCD challenges by providing a diverse and accurately labeled dataset for model training and evaluation.

5) *xBD* [42]: The xBD dataset, pivotal for advancing CD and BDA in disaster response, integrates pre- and post-disaster satellite imagery with over 850,000 building annotations across 45,362 km². It stands as the largest dataset of its kind, enriched by environmental data and detailed damage levels for a broad spectrum of disaster events. Developed in collaboration with disaster response agencies, xBD is engineered to refine emergency response strategies, including resource allocation and aid distribution. The dataset adheres to stringent criteria, featuring high-resolution imagery (below a 0.8m GSD), encapsulating multiple levels of damage, and covering a diverse

range of disaster types and building structures. By including both damaged and undamaged sites, xBD is crafted to foster the creation of adaptive models that effectively navigate the complexities of various disaster scenarios.

The information of these five datasets is summarized in Table I.

B. Experimental Setup

1) *Implementation Details*: All three of our proposed architectures are implemented in Pytorch. Depending on the size and depth of the encoder network, our proposed MambaBCD, MambaSCD, and MambaBDA architectures are available in Tiny, Small, and Base versions [30]. As shown in Table II, the difference between them is the number of VSS blocks inside each stage and the number of channels in the feature map. For datasets other than the SYSU dataset, the multi-temporal image pairs and associated labels are cropped to 256×256 pixels for input to the network, and then the data with the original size is inferred using the trained networks on the test set. During training, we optimized the network using the AdamW optimizer [57] with a learning rate of $1e^{-4}$ and weight decay of $5e^{-3}$, without any learning rate decay strategy. The batch size is set to 16. Except for the SYSU dataset where we set the number of training iterations to 20000, we set the number of training iterations to 50000 on the remaining four datasets. The random rotation, left-right, and top-bottom flip are used as training data augmentation methods. Our source code will be open-sourced¹ for community reproduction and subsequent research.

2) *Assessment Metrics*: For evaluating model performance across different CD subtasks, we employ a set of metrics tailored to the specific requirements of BCD, SCD, and BDA.

In assessing BCD, we use the following metrics:

- **Recall (Rec)**: The proportion of actual positives that were correctly identified is measured by the recall, defined as

$$Rec = \frac{TP}{TP + FN}, \quad (11)$$

where TP represents true positives and FN denotes false negatives.

- **Precision (Pre)**: Reflecting the accuracy of positive predictions, precision is defined as

$$Pre = \frac{TP}{TP + FP}, \quad (12)$$

with FP standing for false positives.

- **Overall Accuracy (OA)**: The ratio of correctly predicted observations to the total observations is represented by

$$OA = \frac{TP + TN}{TP + TN + FP + FN}, \quad (13)$$

where TN indicates true negatives.

- **F1 Score (F1)**: Balancing both precision and recall, harmonic mean, given by

$$F1 = 2 \times \frac{Pre \times Rec}{Pre + Rec}, \quad (14)$$

¹<https://github.com/ChenHongruixuan/MambaCD>

TABLE I: Information of the five benchmark datasets used for experiments.

Dataset	Study site	Number of image pairs	Image size	Spatial resolution	Evaluation task
SYSU	Hong Kong	20,000	256 × 256	0.5m	BCD (class-agnostic)
LEVIR-CD+	Texas of the US	985	1,024 × 1,024	0.5m	BCD (single-object)
WHU-CD	Christchurch, New Zealand	2	21,243/11,265 × 15,354	0.3m	BCD (single-object)
SECOND	Hangzhou, Chengdu, and Shanghai	4,662	512 × 512	0.5-3m	SCD
xBD	15 countries	22,068	1,024 × 1,024	<0.8m	BDA

TABLE II: Number of layers and feature channels for encoders in ChangeMamba series.

Stage	Tiny	Small	Base
I	$L_1 = 2$	$L_1 = 2$	$L_1 = 2$
	$C_1 = 96$	$C_1 = 96$	$C_1 = 128$
II	$L_2 = 2$	$L_2 = 2$	$L_2 = 2$
	$C_2 = 192$	$C_2 = 192$	$C_2 = 256$
III	$L_3 = 9$	$L_3 = 27$	$L_2 = 27$
	$C_3 = 384$	$C_3 = 384$	$C_3 = 512$
IV	$L_4 = 2$	$L_4 = 2$	$L_4 = 2$
	$C_4 = 768$	$C_4 = 768$	$C_4 = 1024$

- **Intersection over Union (IoU):** Also known as the Jaccard index, this metric measures the overlap between the predicted and actual positives:

$$IoU = \frac{TP}{TP + FP + FN}, \quad (15)$$

- **Cohen's Kappa (κ_c):** Assessing the agreement between two raters beyond chance, Cohen's Kappa is given by

$$\kappa_c = \frac{p_o - p_e}{1 - p_e}, \quad (16)$$

where p_o is the observed agreement, and p_e is the expected agreement by chance.

For SCD, the metrics used include:

- **Overall Accuracy (OA) and F1 Score (F1):** As defined for BCD.
- **Mean Intersection over Union (mIoU):** Averaging IoU across classes, mIoU is calculated as

$$mIoU = \frac{1}{N} \sum_{i=1}^N \frac{TP_i}{TP_i + FP_i + FN_i}, \quad (17)$$

aiming to provide a balanced measure across different classes.

- **Separated Kappa (SeK) coefficient:** Specifically proposed in [38] to alleviate the influences of label imbalance in SCD model evaluation, SeK is defined in a cited work.

For BDA, we follow the protocol of xView2 Challenge to split BDA into two subtasks, i.e., building localization and damage classification tasks. The following metrics are adopted to measure the performance of each subtask and the overall BDA performance:

- **F1 Score for Localization (F_1^{loc}) and Classification (F_1^{clf}):** These metrics assess accuracy in building localization and damage classification, respectively.

- **Overall F1 Score ($F_1^{overall}$):** This reflects the combined performance in both building localization and damage classification tasks.

- **F1 Score for Different Damage Level Classes (F_1^{level}):** This evaluates the model's performance across various damage extents.

Employing this collectively comprehensive set of metrics ensures a balanced and thorough evaluation, offering a detailed assessment of the model's capabilities across a range of CD tasks.

C. Comparison Methods

To rigorously assess the performance of Mamba in CD tasks, we strategically selected a diverse range of methods based on CNN and Transformer architectures for benchmarking across three distinct tasks: BCD, SCD, and BDA.

For BCD, our comparison includes a suite of CNN-based methodologies: FC-EF [16], FC-Siam-Diff [16], FC-Siam-Conc [16], and SiamCRNN [13] (utilizing ResNet architectures ranging from ResNet-18 to ResNet-101), alongside SNUNet [32], DSIFN [17], HANet [33], and CGNet [34]. On the Transformer front, we compare against ChangeFormer (versions 1 to 4) [22], BIT (with ResNet-18 to ResNet-101 as the backbone for feature extraction) [20], TransUNetCD [25], and SwinSUNet [24].

In the SCD arena, CNN-based competitors encompass HRSCD (variants S1 to S4) [35], ChangeMask [18], SSCD-1 [39], Bi-SRNet [39], and TED [45]. For Transformer-based methodologies, we evaluate against SMNet [44] and ScanNet [45].

Lastly, for the BDA task, we selected the xView2 baseline [42], Siamese-UNet (the winning solution of the xView2 challenge) [42], MaskRCNN [43], and ChangeOS [3] (employing ResNet-18 to ResNet-101) as CNN-based benchmarks. DamFormer [23] stands as the solitary Transformer-based comparison method.

For the above methods, if the detection performance was reported in the original paper on the corresponding dataset, we directly adopt the accuracy in the original paper. If not, we train and test the method on the corresponding dataset based on the hyperparameters recommended in the original paper, using the loss function and data augmentation methods consistent with our method.

D. Benchmark Comparison in Three CD Subtasks

- 1) **BCD:** Tables III to V list the performance in BCD of the proposed MambaBCD architecture and some comparison

TABLE III: Accuracy assessment for different binary CD models on the SYSU dataset, where \mathcal{C} indicates CNN-based models, \mathcal{T} indicates Transformer-based models, and \mathcal{M} indicates Mamba-based models. The table highlights the highest values in red, and the second-highest results in blue

Type	Method	Rec	Pre	OA	F1	IoU	KC
\mathcal{C}	FC-EF [16]	75.17	76.47	88.69	75.81	61.04	68.43
	FC-Siam-Diff [16]	75.30	76.28	88.65	75.79	61.01	68.38
	FC-Siam-Conc [16]	76.75	73.67	88.05	75.18	60.23	67.32
	SiamCRNN-18 [13]	76.83	84.80	91.29	80.62	67.54	75.02
	SiamCRNN-34 [13]	76.85	85.13	91.37	80.78	67.75	75.23
	SiamCRNN-50 [13]	78.40	83.41	91.23	80.83	67.82	75.15
	SiamCRNN-101 [13]	80.48	80.40	90.77	80.44	67.28	74.40
	SNUNet [32]	72.21	74.09	87.49	73.14	57.66	64.99
	DSIFN [17]	82.02	75.83	89.59	78.80	65.02	71.92
	HANet [33]	76.14	78.71	89.52	77.41	63.14	70.59
	CGNet [34]	74.37	86.37	91.19	79.92	66.55	74.31
\mathcal{T}	ChangeFormerV1 [22]	75.82	79.65	89.73	77.69	63.52	71.02
	ChangeFormerV2 [22]	75.62	78.14	89.26	76.86	62.42	69.87
	ChangeFormerV3 [22]	75.24	79.46	89.57	77.29	62.99	70.53
	ChangeFormerV4 [22]	77.90	79.74	90.12	78.81	65.03	72.37
	BIT-18 [20]	76.42	84.85	91.22	80.41	67.24	74.78
	BIT-34 [20]	74.63	82.40	90.26	78.32	64.37	72.06
	BIT-50 [20]	77.90	81.42	90.60	79.62	66.14	73.51
\mathcal{M}	BIT-101 [20]	75.58	83.64	90.76	79.41	65.84	73.47
	TransUNetCD [25]	77.73	82.59	90.88	80.09	66.79	74.18
	SwinSUNet [24]	79.75	83.50	91.51	81.58	68.89	76.06
	MambaBCD-Tiny	79.59	83.06	91.36	81.29	68.48	75.68
	MambaBCD-Small	78.25	87.99	92.35	82.83	70.70	77.94
	MambaBCD-Base	80.31	86.11	92.30	83.11	71.10	78.13

methods on the three benchmark datasets. In these tables, we differentiate between the types of these BCD architectures into CNN-based methods, Transformer-based methods, and our Mamba-based methods. It can be seen that our approaches significantly outperform either the CNN-based approaches or the Transformer-based architectures. The proposed MambaBCD-Base and MambaBCD-Small architectures achieve the highest and second-highest OA, F1, IoU, and KC for both class-agnostic CD (SYSU dataset) and single-object CD tasks (LEVIR-CD+ and WHU-CD datasets), fully demonstrating the potential of the Mamba architecture for the BCD task. Fig. 7 to Fig. 9 then show some binary change maps predicted by our three architectures on the test sets of the three datasets. It can be seen that the proposed methods accurately detect changes with varying types, scales, and numbers contained in these image pairs, very close to the change reference maps.

Table VI lists the network parameters and GFLOPs of these BCD architectures. Benefiting from the S6 model, the MambaBCD architecture can have only linear computational complexity while modeling global context information. It can be seen that even the largest model MambaBCD-Base has GFLOPs of 179.32, which is lower than many CNN and Transformer architectures, like DSIFN, CFNet, and ChangeFormerV4, comparable to some CNN SOTA methods such as SNUNet and SiamCRNN-50. However, the accuracy advantage is obvious. In particular, the MambaBCD-Tiny architecture has a clear accuracy advantage over other architectures with a similar number of parameters and computational con-

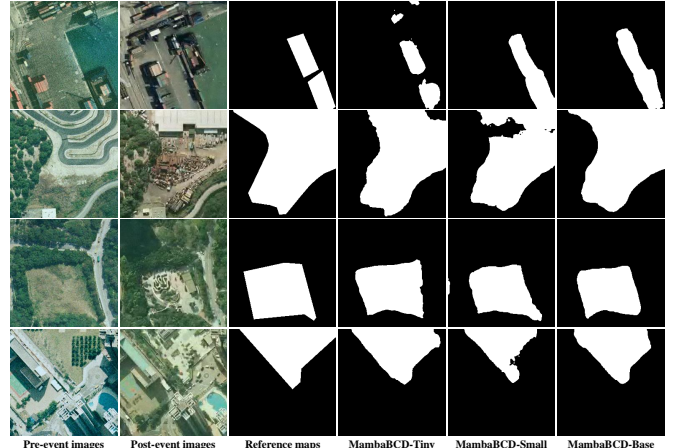


Fig. 7: Some binary change maps obtained by our methods on the test set of the SYSU dataset.

sumption. For example, compared to BIT-18, MambaBCD-Tiny has 56.9% lower GFLOPs but 0.88%, 1.33% and 3.00% higher F1 scores on the three datasets.

2) *SCD*: Table VII compares the SCD performance of the proposed MamabaSCD architectures and representative SCD approaches. Compared to the BCD task, the SCD task requires the change detector capable of effectively modeling not only the spatio-temporal relationships of multi-temporal images, but also learning representative and discriminative

TABLE IV: Accuracy assessment for different binary CD models on the LEVIR-CD+ dataset, where \mathcal{C} indicates CNN-based models, \mathcal{T} indicates Transformer-based models, and \mathcal{M} indicates Mamba-based models. The table highlights the highest values in **red**, and the second-highest results in **blue**

Type	Method	Rec	Pre	OA	F1	IoU	KC
\mathcal{C}	FC-EF [16]	71.77	69.12	97.54	70.42	54.34	69.14
	FC-Siam-Diff [16]	74.02	81.49	98.26	77.57	63.36	76.67
	FC-Siam-Conc [16]	78.49	78.39	98.24	78.44	64.53	77.52
	SiamCRNN-18 [13]	84.25	81.22	98.56	82.71	70.52	81.96
	SiamCRNN-34 [13]	83.88	82.28	98.61	83.08	71.05	82.35
	SiamCRNN-50 [13]	81.61	85.39	98.68	83.46	71.61	82.77
	SiamCRNN-101 [13]	80.96	85.56	98.67	83.20	71.23	82.50
	DSIFN [17]	84.36	83.78	98.70	84.07	72.52	83.39
	SNUNet [32]	78.73	71.07	97.83	74.70	59.62	73.57
	HANet [33]	75.53	79.70	98.22	77.56	63.34	76.63
\mathcal{T}	CGNet [34]	86.02	81.46	98.63	83.68	71.94	82.97
	ChangeFormerV1 [22]	77.00	82.18	98.38	79.51	65.98	78.66
	ChangeFormerV2 [22]	81.32	79.10	98.36	80.20	66.94	79.35
	ChangeFormerV3 [22]	79.97	81.34	98.44	80.65	67.58	79.84
	ChangeFormerV4 [22]	76.68	75.07	98.01	75.87	61.12	74.83
	BIT-18 [20]	80.86	83.76	98.58	82.28	69.90	81.54
	BIT-34 [20]	80.96	85.87	98.68	83.34	71.44	82.66
	BIT-50 [20]	81.84	85.02	98.67	83.40	71.53	82.71
	BIT-101 [20]	81.20	83.91	98.60	82.53	70.26	81.80
	TransUNetCD [25]	84.18	83.08	98.66	83.63	71.86	82.93
\mathcal{M}	SwinSUNet [24]	85.85	85.34	98.92	85.60	74.82	84.98
	MambaBCD-Tiny	81.79	85.51	98.69	83.61	71.83	82.93
	MambaBCD-Small	86.49	89.17	99.02	87.81	78.27	87.30
	MambaBCD-Base	87.57	89.24	99.06	88.39	79.20	87.91

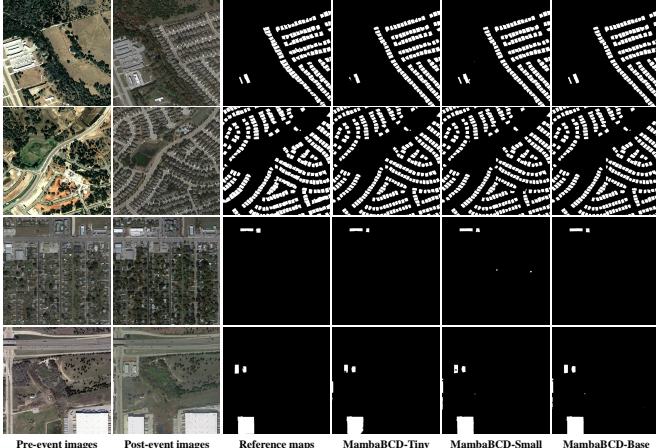


Fig. 8: Some binary change maps obtained by our methods on the test set of the LEVIR-CD+ dataset.

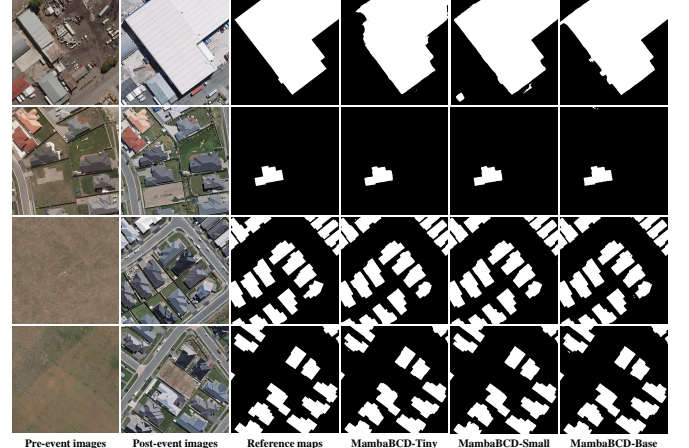


Fig. 9: Some binary change maps obtained by our methods on the test set of the WHU-CD dataset.

representations for accurate land-cover mapping. From Table VII, we can see that the MambaSCD architecture can satisfy both requirements well. The MambaSCD-Small architecture surpasses the Transformer-based SOTA approach, ScanNet, on all four metrics of the SCD task, with OA of 88.38%, F1 of 64.10%, mIoU of 73.61%, and SeK of 24.04 %. Note that our methods have achieved the current accuracy without employing loss functions such as those proposed for the SCD task in ScanNet [45]. Table VIII further lists the number of parameters

and GFLOPs of these methods. Compared to the Transformer-based ScanNet method, the GFLOPs of our three architectures are lower. Compared to SMNet, another Transformer-based method, the proposed MamabaSCD-Tiny can achieve higher SeK values with lower number of parameters and GFLOPs. These results demonstrate the effectiveness of the proposed methods and the potential of the Mamba architecture on the SCD task.

Fig. 10 shows some semantic change maps on the test

TABLE V: Accuracy assessment for different binary CD models on the WHU-CD dataset, where \mathcal{C} indicates CNN-based models, \mathcal{T} indicates Transformer-based models, and \mathcal{M} indicates Mamba-based models. The table highlights the highest values in **red**, and the second-highest results in **blue**

Type	Method	Rec	Pre	OA	F1	IoU	KC
\mathcal{C}	FC-EF [16]	86.33	83.50	98.87	84.89	73.74	84.30
	FC-Siam-Diff [16]	84.69	90.86	99.13	87.67	78.04	87.22
	FC-Siam-Conc [16]	87.72	84.02	98.94	85.83	75.18	85.28
	SiamCRNN-18 [13]	90.48	91.56	99.34	91.02	83.51	90.68
	SiamCRNN-34 [13]	89.10	93.88	99.39	91.42	84.20	91.11
	SiamCRNN-50 [13]	91.45	86.70	99.30	90.57	82.76	90.20
	SiamCRNN-101 [13]	90.45	87.79	99.19	89.10	80.34	88.68
	DSIFN [17]	83.45	97.46	99.31	89.91	81.67	89.56
	SNUNet [32]	87.36	88.04	99.10	87.70	78.09	87.23
	HANet [33]	88.30	88.01	99.16	88.16	78.82	87.72
\mathcal{T}	CGNet [34]	90.79	94.47	99.48	92.59	86.21	92.33
	ChangeFormerV1 [22]	84.30	90.80	99.11	87.43	77.67	86.97
	ChangeFormerV2 [22]	83.41	88.77	99.00	86.00	75.45	85.49
	ChangeFormerV3 [22]	85.55	88.25	99.05	86.88	76.80	86.39
	ChangeFormerV4 [22]	84.85	90.09	99.10	87.39	77.61	86.93
	BIT-18 [20]	90.36	90.30	99.29	90.33	82.37	89.96
	BIT-34 [20]	90.10	89.14	99.23	89.62	81.19	89.22
	BIT-50 [20]	90.33	89.70	99.26	90.01	81.84	89.63
	BIT-101 [20]	90.24	89.83	99.27	90.04	81.88	89.66
	TransUNetCD [25]	90.50	85.48	99.09	87.79	78.44	87.44
\mathcal{M}	SwinSUNet [24]	92.03	94.08	99.50	93.04	87.00	92.78
	MambaBCD-Tiny	91.94	94.76	99.52	93.33	87.49	93.08
	MambaBCD-Small	92.29	95.90	99.57	94.06	88.79	93.84
	MambaBCD-Base	92.23	96.18	99.58	94.19	89.02	93.98

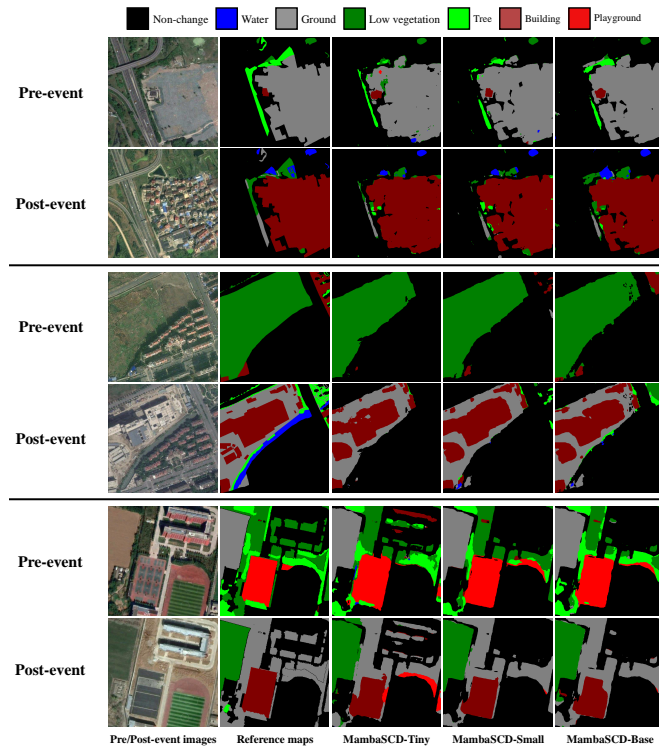


Fig. 10: Some semantic change maps obtained by the proposed MambaSCD architectures on the test set of the SECONd dataset.

set of the SECONd dataset. Due to land-cover category combinations, SCD often involves a considerable number of categories. For ease of visualization, we follow the visualization way in [18], [38], [58], namely only plotting the land-cover categories of the changed regions in both pre- and post-event images. In this way, the “from-to” semantic change information can be effectively reflected. From Fig. 10, we can observe that the MambaSCD architecture is not only capable of distinguishing changed features at different scales, but also accurately identifying the specific semantic categories of these changes.

3) **BDA:** Table IX reports the accuracy of the MambaBDA architecture and some Transformer and CNN-based architectures on the xBD dataset. The performance of MambaBDA architecture significantly outperforms these representative BDA approaches. Compared to the current Transformer-based SOTA method, DamFormer [23], our three MambaBDA architectures have a 2.64%, 4.12%, and 4.39% higher $F_1^{overall}$, respectively. Moreover, it can be noticed that the accuracy improvement compared to DamFormer mainly comes from the more difficult damage classification task rather than the building localization task, which demonstrates that the proposed MambaBDA architecture can adequately learn the spatio-temporal relationships between the multi-temporal images so as to effectively distinguish different building damage levels.

Fig. 11 shows the visualization results of building damages caused by different disaster events obtained by MambaBDA on the xBD dataset. MambaBDA can accurately localize and

TABLE VI: Comparison of different binary CD models in computational cost, where \mathcal{C} indicates CNN-based models, \mathcal{T} indicates Transformer-based models, and \mathcal{M} indicates Mamba-based models

Type	Method	Params (M)	GFLOPs
\mathcal{C}	FC-EF [16]	1.35	14.13
	FC-Siam-Diff [16]	1.35	18.66
	FC-Siam-Conc [16]	1.54	21.07
	SiamCRNN-18 [13]	18.85	86.64
	SiamCRNN-34 [13]	28.96	113.28
	SiamCRNN-50 [13]	44.45	185.30
	SiamCRNN-101 [13]	63.44	224.30
	DSIFN [17]	35.73	329.03
	SNUNet [32]	10.21	176.36
	HANet [33]	2.61	70.68
\mathcal{T}	CGNet [34]	33.68	329.58
	ChangeFormerV1 [22]	29.84	46.62
	ChangeFormerV2 [22]	24.30	44.54
	ChangeFormerV3 [22]	24.30	33.68
	ChangeFormerV4 [22]	33.61	852.53
	TransUNetCD [25]	28.37	244.54
	SwinSUNet [24]	39.28	43.50
	BIT-18 [20]	11.50	106.14
	BIT-34 [20]	21.61	190.83
	BIT-50 [20]	24.28	224.61
\mathcal{M}	BIT-101 [20]	43.27	380.62
	MambaBCD-Tiny	17.13	45.74
	MambaBCD-Small	49.94	114.82
	MambaBCD-Base	84.70	179.32

TABLE VII: Accuracy assessment for different SCD models on the SECOND dataset, where \mathcal{C} indicates CNN-based models, \mathcal{T} indicates Transformer-based models, and \mathcal{M} indicates Mamba-based models. The table highlights the highest values in red, and the second-highest results in blue

Type	Method	OA	F1	mIoU	SeK
\mathcal{C}	HRSCD-S1 [35]	45.77	38.44	62.72	5.90
	HRSCD-S2 [35]	85.49	49.22	64.43	10.69
	HRSCD-S3 [35]	84.62	51.62	66.33	11.97
	HRSCD-S4 [35]	86.62	58.21	71.15	18.80
	ChangeMask [18]	86.93	59.74	71.46	19.50
	SSCD-1 [39]	87.19	61.22	72.60	21.86
	Bi-SRNet [39]	87.84	62.61	73.41	23.22
	TED [45]	87.39	60.34	72.79	22.17
	SMNet [44]	86.68	60.34	71.95	20.29
	ScanNet [45]	87.86	63.66	73.42	23.94
\mathcal{M}	MamabaSCD-Tiny	87.22	60.92	72.18	20.92
	MamabaSCD-Small	88.38	64.10	73.61	24.04
	MamabaSCD-Base	88.00	63.98	73.47	23.94

then differentiate the damage levels of buildings despite the varying type of building and the disaster event, implying the potential of the MambaBDA architecture for practical disaster response applications.

TABLE VIII: Comparison of different SCD models in computational cost, where \mathcal{C} indicates CNN-based models, \mathcal{T} indicates Transformer-based models, and \mathcal{M} indicates Mamba-based models.

Type	Method	Params	GFLOPs
\mathcal{C}	HRSCD-S1 [35]	3.36	8.02
	HRSCD-S2 [35]	6.39	14.29
	HRSCD-S3 [35]	12.77	42.67
	HRSCD-S4 [35]	13.71	43.69
	ChangeMask [18]	2.97	37.16
	SSCD-1 [39]	23.31	189.57
	Bi-SRNet [39]	23.39	189.91
	TED [45]	24.19	204.29
	SMNet [44]	42.16	75.79
	ScanNet [45]	27.90	264.95
\mathcal{M}	MamabaSCD-Tiny	19.44	63.72
	MamabaSCD-Small	51.82	137.10
	MamabaSCD-Base	87.47	201.85

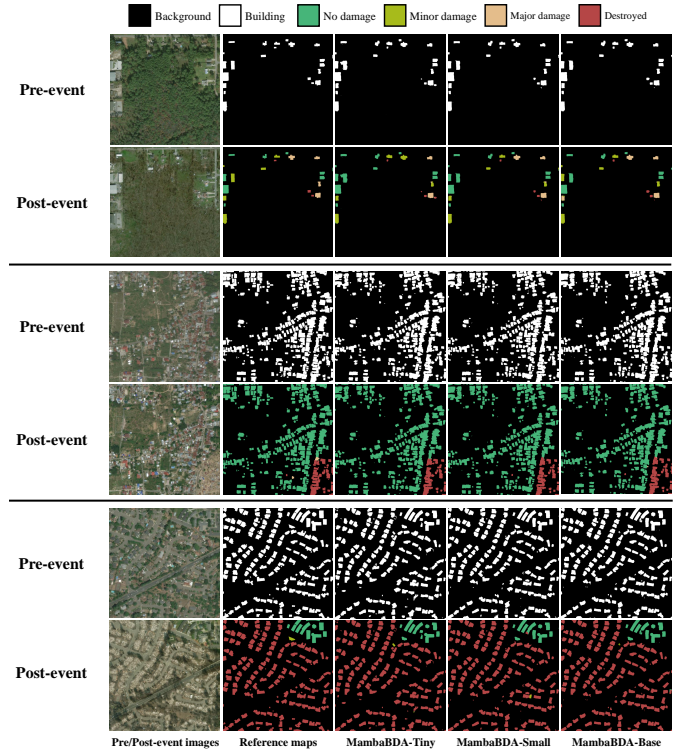


Fig. 11: Some building damage assessment results obtained by our methods on the test set of the xBD dataset. From top to bottom, the disaster events are typhoons, tsunamis, and wildfires.

E. Different Spatio-Temporal Fusion Methods

Modelling spatio-temporal relationships is significant to CD tasks [13], [18], [36]. To demonstrate the effectiveness of our proposed CST-Mamba module, we compare it with several commonly used spatial-temporal modeling methods in CD. They are concatenation operations with feature pyramid network (FPN) [18] (baseline), temporal-symmetric transformer based on 3D convolution layers (TST) [18], RNN-based method [13], and Transformer-based method [20]. Table X lists the performance of these modeling methods on the three CD

TABLE IX: Accuracy assessment for different building damage assessment models on the xBD dataset, where \mathcal{C} indicates CNN-based models, \mathcal{T} indicates Transformer-based models, and \mathcal{M} indicates Mamba-based models. The table highlights the highest values in **red**, and the second-highest results in **blue**. The suffix PPS means post-processing.

Type	Method	F_1^{loc}	F_1^{clf}	$F_1^{overall}$	Damage F_1 per class			
					No damage	Minor damage	Major damage	Destroyed
\mathcal{C}	xView2 Baseline	80.47	3.42	26.54	66.31	14.35	0.94	46.57
	Siamese-UNet	85.92	65.58	71.68	86.74	50.02	64.43	71.68
	MaskRCNN [43]	83.60	70.02	74.10	90.60	49.30	72.20	83.70
	ChangeOS-18 [3]	84.62	69.87	74.30	88.61	52.10	70.36	79.65
	ChangeOS-34 [3]	85.16	70.28	74.74	88.63	52.38	71.16	80.08
	ChangeOS-50 [3]	85.41	70.88	75.24	88.98	53.33	71.24	80.60
	ChangeOS-101 [3]	85.69	71.14	75.50	89.11	53.11	72.44	80.79
	ChangeOS-18-PPS [3]	84.62	73.89	77.11	92.38	57.41	72.54	82.62
	ChangeOS-34-PPS [3]	85.16	74.25	77.52	92.19	58.07	72.84	82.79
\mathcal{T}	ChangeOS-50-PPS [3]	85.41	75.64	78.57	92.66	60.14	74.18	83.45
	ChangeOS-101-PPS [3]	85.69	75.44	78.52	92.81	59.38	74.65	83.29
	DamFormer [23]	86.86	72.81	77.02	89.86	56.78	72.56	80.51
\mathcal{M}	MambaBDA-Tiny	84.76	77.50	79.68	95.33	60.15	75.94	88.27
	MambaBDA-Small	86.61	78.80	81.14	95.99	62.82	76.26	88.37
	MambaBDA-Base	87.38	78.84	81.41	95.94	62.74	76.46	88.58

TABLE X: Comparison of different approaches for modeling spatio-temporal relationships on three tasks. The table highlights the highest values in **red**, and the second-highest results in **blue**.

Method	SYSU				SECOND				xBD			
	OA	F1	IoU	KC	OA	F1	mIoU	SeK	F_1^{loc}	F_1^{clf}	$F_1^{overall}$	
Baseline	91.71	81.11	68.22	75.84	87.85	62.71	72.33	22.14	84.85	74.74	77.77	
STT [18]	92.09	82.22	69.80	77.16	88.09	63.36	73.01	23.11	86.74	75.92	79.17	
RNN [13]	92.97	82.02	69.52	76.94	88.20	63.63	72.86	23.09	85.74	76.48	79.26	
Transformer [20]	92.14	82.17	69.74	77.17	88.05	64.05	73.02	23.44	86.09	77.45	80.04	
Ours	92.35	82.83	70.70	77.94	88.38	64.10	73.61	24.04	86.61	78.80	81.14	

subtasks. On the simpler BCD tasks, Transformer does not yield significant advantages in performance compared to RNN. However, on the more difficult SCD and BDA tasks, the advantages of the Transformer architecture are illustrated. Compared with these current representative spatio-temporal relationship modeling approaches, our proposed cross-temporal modeling approach based on Mamba, which inherits the advantages of RNN and Transformer, shows superior performance on the three CD tasks of BCD, SCD, and BDA. Compared to the Transformer-based spatio-temporal modeling approach, our method improves the F1 value by 0.77% on BCD, SeK by 0.6% on the SCD task, and $F_1^{overall}$ by 1.10% on the BDA task.

In addition, We further visualize the features extracted by the MambaBCD architecture in Fig. 12. In the features extracted by the encoder, the features in the region of high response values are not necessarily regions of interest, i.e., changed regions. Whereas, in the decoder, after the spatio-temporal relationships are gradually modeled by the proposed CST-Mamba modules, changed regions gradually exhibit high response values.

F. Comparison to Other Backbone Networks

Finally, we simply compare the Mamba with some representative backbone networks in CD tasks on the SYSU

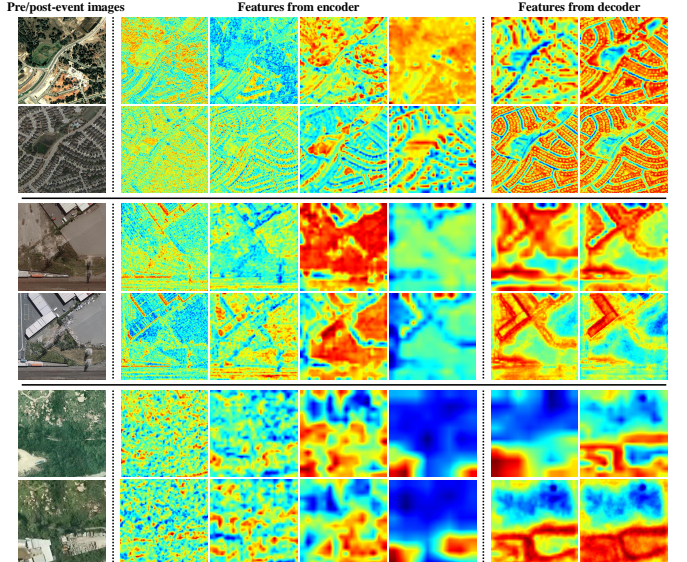


Fig. 12: The visualization of features from different layers of MambaBCD.

dataset in Table XI. It can be seen that Mamba outperforms the two Transformer backbone networks, Swin-Transformer and MixFormer. This is because, in order to reduce the

TABLE XI: Comparison of different commonly used backbones in BCD on the SYSU dataset. The table highlights the highest values in **red**, and the second-highest results in **blue**.

Encoder	OA	F1	IoU	KC	Params	GFLOPs
ResNet-101	91.10	81.10	68.22	75.28	46.90	131.36
EfficientNet-B5	91.60	82.26	69.86	76.84	6.55	53.62
MixFormer-v3	87.70	75.00	60.00	66.87	47.03	82.98
Swin-Small	92.09	82.22	69.80	77.16	36.22	81.72
Mamba-Small	92.35	82.83	70.70	77.94	49.94	114.82

computational overhead of self-attention operation, these two Transformer backbone networks either adopt a local attention mechanism (Swin-Transformer) [26] or a strided convolution layer (MixFormer) [27] to reduce the size of the feature maps, which will negatively affect the learning of global contextual information. The Mamba architecture, on the other hand, can reduce its computational consumption to a linear relationship with the number of tokens, thus eliminating the need for these methods, which cause information loss, and allowing the fully learning of global context information. As for the remote sensing change detection task, due to the multi-scale phenomenon of land-cover features and the differences in spatial resolution of different sensors, the sizes of changed objects often vary greatly. Therefore, the features extracted by Mamba through fully learning the global contextual information, are particularly important for the subsequent detection of these changed objects with different sizes.

V. CONCLUSION

In this paper, we explore the potential of the emerging Mamba architecture for remote sensing image change detection tasks. Three architectures, MambaBCD, MambaSCD, and MambaBDA are developed for binary change detection, semantic change detection, and building damage assessment tasks, respectively. The encoders of all three architectures are cutting-edge visual Mamba, which can adequately learn the global contextual information of the input image with linear complexity. Then, for the decoder, in order to adequately learn about spatio-temporal relations, we propose three ways of modeling spatio-temporal relations which can adequately exploiting the attributes and advantages of Mamba architecture. Experiments on five benchmark datasets have fully revealed the potential of Mamba for multi-temporal remote sensing image data processing tasks. Compared to the CNN-based and Transformer-based approaches, the proposed three architectures can achieve SOTA performance on their respective tasks. Compared to some commonly used backbone networks, the Mamba architecture can extract features that are more suitable for downstream CD tasks. The combination of our proposed three spatio-temporal relationship modeling mechanisms and the Mamba architecture provides a new perspective on modeling spatio-temporal relationships, showing much better detection results on all three subtasks.

Our future work includes, but is not limited to, developing Mamba architectures more suited to the characteristics of remote sensing data and exploring the potential of Mamba for multimodal remote sensing tasks.

REFERENCES

- [1] D. Lu, P. Mausel, E. Brondízio, and E. Moran, “Change detection techniques,” *Int. J. Remote Sens.*, vol. 25, no. 12, pp. 2365–2407, 2004.
- [2] P. Coppin, I. Jonckheere, K. Nackaerts, B. Muys, and E. Lambin, “Digital change detection methods in ecosystem monitoring: A review,” *Int. J. Remote Sens.*, vol. 25, no. 9, pp. 1565–1596, 2004.
- [3] Z. Zheng, Y. Zhong, J. Wang, A. Ma, and L. Zhang, “Building damage assessment for rapid disaster response with a deep object-based semantic change detection framework: From natural disasters to man-made disasters,” *Remote Sens. Environ.*, vol. 265, p. 112636, 2021.
- [4] H. Guo, Q. Shi, A. Marinoni, B. Du, and L. Zhang, “Deep building footprint update network: A semi-supervised method for updating existing building footprint from bi-temporal remote sensing images,” *Remote Sens. Environ.*, vol. 264, p. 112589, 2021.
- [5] H. Chen, N. Yokoya, C. Wu, and B. Du, “Unsupervised Multimodal Change Detection Based on Structural Relationship Graph Representation Learning,” *IEEE Trans. Geosci. Remote Sens.*, pp. 1–18, 2022.
- [6] H. Chen, C. Lan, J. Song, C. Broni-Bediako, J. Xia, and N. Yokoya, “Land-cover change detection using paired openstreetmap data and optical high-resolution imagery via object-guided transformer,” *arXiv preprint arXiv:2310.02674*, 2023.
- [7] C. Wu, B. Du, and L. Zhang, “Slow feature analysis for change detection in multispectral imagery,” *IEEE Trans. Geosci. Remote Sens.*, vol. 52, no. 5, pp. 2858–2874, 2014.
- [8] A. A. Nielsen, “The regularized iteratively reweighted MAD method for change detection in multi- and hyperspectral data,” *IEEE Trans. Image Process.*, vol. 16, no. 2, pp. 463–478, 2007.
- [9] L. Bruzzone and Diego Fernández Prieto, “Automatic Analysis of the Difference Image for Unsupervised Change Detection,” *IEEE Trans. Geosci. Remote Sens.*, vol. 38, no. 3, pp. 1171–1182, 2000.
- [10] M. Hussain, D. Chen, A. Cheng, H. Wei, and D. Stanley, “Change detection from remotely sensed images: From pixel-based to object-based approaches,” *ISPRS J. Photogramm. Remote Sens.*, vol. 80, pp. 91–106, 2013.
- [11] C. Wu, H. Chen, B. Du, and L. Zhang, “Unsupervised change detection in multitemporal vhr images based on deep kernel pca convolutional mapping network,” *IEEE Trans. Cybern.*, vol. 52, no. 11, pp. 12 084–12 098, 2022.
- [12] M. Gong, T. Zhan, P. Zhang, and Q. Miao, “Superpixel-based difference representation learning for change detection in multispectral remote sensing images,” *IEEE Trans. Geosci. Remote Sens.*, vol. 55, no. 5, pp. 2658–2673, 2017.
- [13] H. Chen, C. Wu, B. Du, L. Zhang, and L. Wang, “Change Detection in Multisource VHR Images via Deep Siamese Convolutional Multiple-Layers Recurrent Neural Network,” *IEEE Trans. Geosci. Remote Sens.*, vol. 58, no. 4, pp. 2848–2864, 2020.
- [14] H. Chen, C. Wu, B. Du, and L. Zhang, “Deep Siamese Multi-scale Convolutional Network for Change Detection in Multi-Temporal VHR Images,” in *2019 10th International Workshop on the Analysis of Multitemporal Remote Sensing Images (MultiTemp)*, 2019, pp. 1–4.
- [15] Q. Shi, M. Liu, S. Li, X. Liu, F. Wang, and L. Zhang, “A deeply supervised attention metric-based network and an open aerial image dataset for remote sensing change detection,” *IEEE Trans. Geosci. Remote Sens.*, vol. 60, pp. 1–16, 2022.
- [16] R. Caye Daudt, B. Le Saux, and A. Boulch, “Fully convolutional siamese networks for change detection,” in *Proceedings - International Conference on Image Processing, ICIP*, 2018, pp. 4063–4067.
- [17] C. Zhang, P. Yue, D. Tapete, L. Jiang, B. Shangguan, L. Huang, and G. Liu, “A deeply supervised image fusion network for change detection in high resolution bi-temporal remote sensing images,” *ISPRS J. Photogramm. Remote Sens.*, vol. 166, no. June, pp. 183–200, 2020.
- [18] Z. Zheng, Y. Zhong, S. Tian, A. Ma, and L. Zhang, “ChangeMask: Deep multi-task encoder-transformer-decoder architecture for semantic change detection,” *ISPRS J. Photogramm. Remote Sens.*, vol. 183, no. March 2021, pp. 228–239, 2022.
- [19] Y. Cao and X. Huang, “A full-level fused cross-task transfer learning method for building change detection using noise-robust pretrained networks on crowdsourced labels,” *Remote Sens. Environ.*, vol. 284, p. 113371, 2023.
- [20] H. Chen, Z. Qi, and Z. Shi, “Remote sensing image change detection with transformers,” *IEEE Trans. Geosci. Remote Sens.*, vol. 60, pp. 1–14, 2022.
- [21] A. Dosovitskiy, L. Beyer, A. Kolesnikov, D. Weissenborn, X. Zhai, T. Unterthiner, M. Dehghani, M. Minderer, G. Heigold, S. Gelly *et al.*, “An image is worth 16x16 words: Transformers for image recognition at scale,” *arXiv preprint arXiv:2010.11929*, 2020.

- [22] W. G. C. Bandara and V. M. Patel, "A transformer-based siamese network for change detection," in *IGARSS 2022 - 2022 IEEE International Geoscience and Remote Sensing Symposium*, 2022, pp. 207–210.
- [23] H. Chen, E. Nemni, S. Vallecorsa, X. Li, C. Wu, and L. Bromley, "Dual-tasks siamese transformer framework for building damage assessment," in *International Geoscience and Remote Sensing Symposium (IGARSS)*, 2022, pp. 1600–1603.
- [24] C. Zhang, L. Wang, S. Cheng, and Y. Li, "Swinsunet: Pure transformer network for remote sensing image change detection," *IEEE Trans. Geosci. Remote Sens.*, vol. 60, pp. 1–13, 2022.
- [25] Q. Li, R. Zhong, X. Du, and Y. Du, "Transunetcd: A hybrid transformer network for change detection in optical remote-sensing images," *IEEE Trans. Geosci. Remote Sens.*, vol. 60, pp. 1–19, 2022.
- [26] Z. Liu, Y. Lin, Y. Cao, H. Hu, Y. Wei, Z. Zhang, S. Lin, and B. Guo, "Swin transformer: Hierarchical vision transformer using shifted windows," in *Proceedings of the IEEE/CVF International Conference on Computer Vision (ICCV)*, October 2021, pp. 10012–10022.
- [27] E. Xie, W. Wang, Z. Yu, A. Anandkumar, J. M. Alvarez, and P. Luo, "Segformer: Simple and efficient design for semantic segmentation with transformers," in *Advances in Neural Information Processing Systems*, vol. 34, 2021, pp. 12077–12090.
- [28] A. Gu, K. Goel, and C. Ré, "Efficiently modeling long sequences with structured state spaces," *arXiv preprint arXiv:2111.00396*, 2021.
- [29] A. Gu and T. Dao, "Mamba: Linear-time sequence modeling with selective state spaces," *arXiv preprint arXiv:2312.00752*, 2023.
- [30] Y. Liu, Y. Tian, Y. Zhao, H. Yu, L. Xie, Y. Wang, Q. Ye, and Y. Liu, "Vmamba: Visual state space model," *arXiv preprint arXiv:2401.10166*, 2024.
- [31] L. Zhu, B. Liao, Q. Zhang, X. Wang, W. Liu, and X. Wang, "Vision mamba: Efficient visual representation learning with bidirectional state space model," *arXiv preprint arXiv:2401.09417*, 2024.
- [32] S. Fang, K. Li, J. Shao, and Z. Li, "Snunet-cd: A densely connected siamese network for change detection of vhr images," *IEEE Geosci. Remote Sens. Lett.*, vol. 19, pp. 1–5, 2022.
- [33] C. Han, C. Wu, H. Guo, M. Hu, and H. Chen, "Hanet: A hierarchical attention network for change detection with bitemporal very-high-resolution remote sensing images," *IEEE Journal of Selected Topics in Applied Earth Observations and Remote Sensing*, vol. 16, pp. 3867–3878, 2023.
- [34] C. Han, C. Wu, H. Guo, M. Hu, J. Li, and H. Chen, "Change guiding network: Incorporating change prior to guide change detection in remote sensing imagery," *IEEE Journal of Selected Topics in Applied Earth Observations and Remote Sensing*, vol. 16, pp. 8395–8407, 2023.
- [35] R. Caye Daudt, B. Le Saux, A. Boulch, and Y. Gousseau, "Multitask learning for large-scale semantic change detection," *Computer Vision and Image Understanding*, vol. 187, p. 102783, 2019.
- [36] L. Mou, L. Bruzzone, and X. X. Zhu, "Learning spectral-spatialoral features via a recurrent convolutional neural network for change detection in multispectral imagery," *IEEE Trans. Geosci. Remote Sens.*, vol. 57, no. 2, pp. 924–935, 2019.
- [37] S. Saha, F. Bovolo, and L. Bruzzone, "Unsupervised deep change vector analysis for multiple-change detection in VHR Images," *IEEE Trans. Geosci. Remote Sens.*, vol. 57, no. 6, pp. 3677–3693, 2019.
- [38] K. Yang, G.-S. Xia, Z. Liu, B. Du, W. Yang, M. Pelillo, and L. Zhang, "Asymmetric siamese networks for semantic change detection in aerial images," *IEEE Trans. Geosci. Remote Sens.*, vol. 60, pp. 1–18, 2022.
- [39] L. Ding, H. Guo, S. Liu, L. Mou, J. Zhang, and L. Bruzzone, "Bitemporal semantic reasoning for the semantic change detection in hr remote sensing images," *IEEE Transactions on Geoscience and Remote Sensing*, vol. 60, pp. 1–14, 2022.
- [40] D. Peng, L. Bruzzone, Y. Zhang, H. Guan, and P. He, "Sednet: A novel convolutional network for semantic change detection in high resolution optical remote sensing imagery," *International Journal of Applied Earth Observation and Geoinformation*, vol. 103, p. 102465, 2021.
- [41] S. Tian, X. Tan, A. Ma, Z. Zheng, L. Zhang, and Y. Zhong, "Temporal-agnostic change region proposal for semantic change detection," *ISPRS Journal of Photogrammetry and Remote Sensing*, vol. 204, pp. 306–320, 2023.
- [42] R. Gupta, B. Goodman, N. Patel, R. Hosfelt, S. Sajeev, E. Heim, J. Doshi, K. Lucas, H. Choset, and M. Gaston, "Creating xbd: A dataset for assessing building damage from satellite imagery," in *Proceedings of the IEEE/CVF Conference on Computer Vision and Pattern Recognition (CVPR) Workshops*, June 2019.
- [43] E. Weber and H. Kané, "Building disaster damage assessment in satellite imagery with multi-temporal fusion," *arXiv preprint arXiv:2004.05525*, 2020.
- [44] Y. Niu, H. Guo, J. Lu, L. Ding, and D. Yu, "Smnet: Symmetric multi-task network for semantic change detection in remote sensing images based on cnn and transformer," *Remote Sensing*, vol. 15, no. 4, 2023.
- [45] L. Ding, J. Zhang, H. Guo, K. Zhang, B. Liu, and L. Bruzzone, "Joint spatio-temporal modeling for semantic change detection in remote sensing images," *IEEE Transactions on Geoscience and Remote Sensing*, vol. 62, pp. 1–14, 2024.
- [46] J. T. Smith, A. Warrington, and S. W. Linderman, "Simplified state space layers for sequence modeling," *arXiv preprint arXiv:2208.04933*, 2022.
- [47] D. Y. Fu, T. Dao, K. K. Saab, A. W. Thomas, A. Rudra, and C. Ré, "Hungry hungry hippos: Towards language modeling with state space models," *arXiv preprint arXiv:2212.14052*, 2022.
- [48] X. He, K. Cao, K. Yan, R. Li, C. Xie, J. Zhang, and M. Zhou, "Pan-mamba: Effective pan-sharpening with state space model," *arXiv preprint arXiv:2402.12192*, 2024.
- [49] K. Chen, B. Chen, C. Liu, W. Li, Z. Zou, and Z. Shi, "Rsmamba: Remote sensing image classification with state space model," *arXiv preprint arXiv:2403.19654*, 2024.
- [50] H. Chen, J. Song, C. Wu, B. Du, and N. Yokoya, "Exchange means change: An unsupervised single-temporal change detection framework based on intra- and inter-image patch exchange," *ISPRS J. Photogramm. Remote Sens.*, vol. 206, pp. 87–105, 2023.
- [51] A. Vaswani, N. Shazeer, N. Parmar, J. Uszkoreit, L. Jones, A. N. Gomez, L. u. Kaiser, and I. Polosukhin, "Attention is all you need," in *Advances in Neural Information Processing Systems*, I. Guyon, U. V. Luxburg, S. Bengio, H. Wallach, R. Fergus, S. Vishwanathan, and R. Garnett, Eds., vol. 30, 2017.
- [52] S. Elfwing, E. Uchibe, and K. Doya, "Sigmoid-weighted linear units for neural network function approximation in reinforcement learning," *Neural networks*, vol. 107, pp. 3–11, 2018.
- [53] T.-Y. Lin, P. Goyal, R. Girshick, K. He, and P. Dollár, "Focal loss for dense object detection," in *Proceedings of the IEEE international conference on computer vision*, 2017, pp. 2980–2988.
- [54] M. Berman, A. R. Triki, and M. B. Blaschko, "The lovász-softmax loss: A tractable surrogate for the optimization of the intersection-over-union measure in neural networks," in *Proceedings of the IEEE Conference on Computer Vision and Pattern Recognition (CVPR)*, June 2018.
- [55] S. Ji, S. Wei, and M. Lu, "Fully convolutional networks for multisource building extraction from an open aerial and satellite imagery data set," *IEEE Transactions on geoscience and remote sensing*, vol. 57, no. 1, pp. 574–586, 2018.
- [56] H. Chen and Z. Shi, "A spatial-temporal attention-based method and a new dataset for remote sensing image change detection," *Remote Sens.*, vol. 12, no. 10, 2020.
- [57] I. Loshchilov and F. Hutter, "Decoupled weight decay regularization," *arXiv preprint arXiv:1711.05101*, 2017.
- [58] S. Tian, Y. Zhong, Z. Zheng, A. Ma, X. Tan, and L. Zhang, "Large-scale deep learning based binary and semantic change detection in ultra high resolution remote sensing imagery: From benchmark datasets to urban application," *ISPRS J. Photogramm. Remote Sens.*, vol. 193, pp. 164–186, 2022.